

## Initial state and thermalization in the Color Glass Condensate framework

Francois Gelis<sup>1</sup>

*Institut de Physique Théorique,  
CEA / DSM / Saclay,  
91191 Gif sur Yvette cedex, France*

In this review, I present the description of the early stages of heavy ion collisions at high energy in the Color Glass Condensate framework, from the pre-collision high energy nuclear wavefunction to the point where hydrodynamics may start becoming applicable.

### 1. Introduction

Heavy ion collisions pose a challenge for Quantum Chromodynamics (QCD) because a comprehensive description of these collisions involves a mix of hard short distance phenomena, and non perturbative long distance soft physics. Even the aspects of these collisions where a hard scale may justify a weak coupling approach are not perturbative in the naive sense of a strict loop expansion. Indeed, resummations are often required even though the coupling is small, usually because the bosonic constituents of the system have a large occupation number that may compensate the smallness of the coupling.

One of the areas where a weak coupling QCD approach is expected to be most effective is the description of the early stages of a heavy ion collision. The term “early stages” usually encompasses the description of the relevant degrees of freedom in the wavefunctions of the two projectiles prior to their collision, the interactions that happen during the very brief duration of the collision itself, and the subsequent evolution of the produced gluons and quarks shortly after the collision. Roughly speaking, the temperature (or the fourth root of the energy density if the system is not yet thermalized) of the system can serve as a measure of the applicability of weak coupling techniques, since this scale sets the value of the running coupling constant.

A lot of progress has been made in the last 20 years in understanding how to apply QCD to these collisions. The starting point was the realization that a hard scale naturally emerges from the non-linear interactions among the gluons when their density is large,<sup>1–3</sup> as is the case in the wavefunction of high energy hadrons or nuclei. Thus, the bulk of particle production in high energy heavy ion collisions is amenable to a weak coupling treatment. The formalism for doing this –known as the Color Glass Condensate (CGC)– was progressively established and refined during this period, and has by now reached a mature state allowing quantitative and systematic calculations.

---

<sup>1</sup>email: francois.gelis@cea.fr

An outstanding problem, that has not yet reached a satisfactory state of understanding, is the transition from the Color Glass Condensate description to a more macroscopic description such as hydrodynamics. The main question is to explain, within the CGC framework, why a hydrodynamical description is possible in the first place. In other words, why does the system produced in a heavy ion collision flow as well as it seems to do? A satisfactory matching between the CGC and hydrodynamics implies that there should be a certain range of time in which the two descriptions predict the same evolution. At the moment, we are not there yet, even though considerable progress has been made in the past years.

After a brief account of why heavy ion collisions are interesting from the point of view of QCD (section 2), the rest of this review follows the time-line of a collision. We recall the main physical ideas behind the parton model in the section 3, and we describe *gluon saturation* in the section 4. The section 5 is devoted to the Color Glass Condensate, the QCD-based effective theory for the saturated regime, and in the section 6 we show how to apply it in order to make leading order calculations in heavy ion collisions. Next-to-Leading order contributions are considered in the section 7, as well as the scale evolution of the gluon distribution in the projectiles via the JIMWLK equation. In the section 8, we first introduce the main issues and puzzles posed by attempts to match CGC calculations and hydrodynamics. In the section 9, we discuss the instabilities that exist in the solutions of the classical Yang-Mills equations, and their disastrous consequences for fixed loop-order CGC predictions beyond leading order. A resummation that cures these pathologies is presented in the section 10, leading to a scheme known as the *Classical Statistical Approximation*. We also present alternative derivations of this approximation scheme in order to make connections with other approaches. We present in the section 11 the results obtained by using this approximation in the context of heavy ion collisions, using different types of initial conditions. A discussion of some known shortcomings of this approximation is presented in the section 12.

## 2. Heavy ion collisions

### 2.1. *Reminder on QCD*

Although they occupy only a tiny fraction of the volume of atoms, the atomic nuclei make up for most of the mass of ordinary matter. The protons and neutrons that are contained in nuclei each contain three valence quarks, that give them their quantum numbers. However, these valence quarks account only for a small part of the nucleon mass. Most of it comes from binding energy, i.e. from the cloud of gluons and virtual quark-antiquark pairs that surrounds the valence quarks. This predominance of binding energy in the mass of hadrons reflects a crucial property of the force which is responsible of the cohesion of hadrons and nuclei: this force becomes strong on distance scales comparable to the proton size, around  $10^{-15}$  m. On the other hand, the measurements of structure functions in deep inelastic scattering experiments,

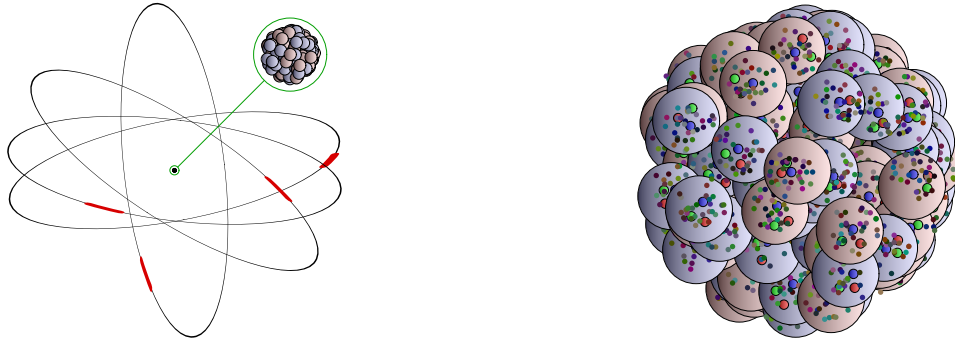


Fig. 1. Atoms and nuclei.

first performed at SLAC in the 1960's, can be understood if one assumes that this force becomes weak on distance scales that are much smaller than the proton size.

The combination of these two properties paved the way to the development of Quantum Chromodynamics (QCD), as the microscopic theory that governs the interactions between quarks and gluons. On the surface, QCD is a gauge theory that resembles very much Quantum Electrodynamics. The matter degrees of freedom are spin 1/2 quarks, that interact by the exchange of vector particles, the gluons.

$$\begin{array}{c} a \\ \color{red}{\text{~~~~~}} \\ \color{green}{\nearrow} \color{green}{\searrow} \\ \color{green}{i} \quad \color{green}{j} \end{array} \sim g(t^a)_{ij} \quad \begin{array}{c} \color{red}{\nearrow} \color{red}{\searrow} \\ \color{red}{a} \quad \color{red}{c} \\ \color{red}{\text{~~~~~}} \\ \color{red}{\nearrow} \color{red}{\searrow} \\ \color{red}{b} \end{array} \sim g(T^a)_{bc} \quad \begin{array}{c} \color{red}{\text{~~~~~}} \\ \color{red}{\text{~~~~~}} \\ \color{red}{\text{~~~~~}} \\ \color{red}{\text{~~~~~}} \\ \color{red}{\text{~~~~~}} \end{array} \quad (1)$$

The quark-gluon coupling in QCD is very similar to the electron-photon coupling in QED, except that it has more “structure” since it involves a matrix of the fundamental representation of SU(3),  $t^a_{ij}$ . In this object, the index  $a$  (running from 1 to 8, the dimension of the SU(3) algebra) is the *color charge* of the gluon, and the indices  $i$  and  $j$  (running from 1 to 3, the dimension of the matrices in the fundamental representation of SU(3)) are the color charges of the incoming and outgoing quarks. The fact that the gluons themselves carry a color charge is the essential difference between QCD and QED, since it leads to novel interaction vertices that involve only gluons. These new interactions are a requirement of gauge symmetry, and can be derived from the following gauge invariant Lagrangian

$$\mathcal{L} = -\frac{1}{4}F^2 + \sum_f \bar{\psi}_f(i\not{D} - m_f)\psi_f . \quad (2)$$

At the classical level, the only free parameters in QCD are the quark masses  $m_f$  and a coupling constant  $g$ . In the quantized theory, the coupling is usually traded for a scale<sup>a</sup>  $\Lambda_{\text{QCD}}$  that emerges from the renormalization of the coupling. This new

<sup>a</sup>Note that, in the absence of quarks (or with only massless quarks), QCD is scale invariant at the classical level. Loop corrections induce a breaking of this scale invariance, which is the reason for the appearance of  $\Lambda_{\text{QCD}}$  in the quantized theory.

scale arises in the running of the coupling constant  $\alpha_s \equiv g^2/(4\pi)$ . At one loop, this is given by<sup>4-8</sup>

$$\alpha_s(E) = \frac{2\pi N_c}{(11N_c - 2N_f) \log(E/\Lambda_{QCD})}, \quad (3)$$

where  $E$  is the energy scale,  $N_c$  the number of colors and  $N_f$  the number of quark flavors. The main difference compared to QED, due to the self-interactions of the

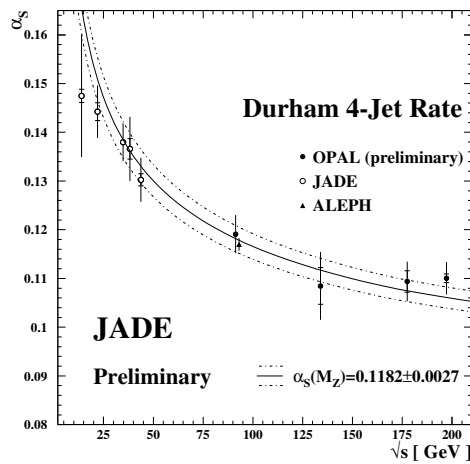


Fig. 2. Running coupling in QCD.

gluons, is the fact that the coupling becomes smaller at short distances as shown in the figure 2, a property known as *asymptotic freedom*.

A related property of QCD is the long distance behavior of the interaction potential between a quark and an antiquark. This can be calculated numerically in lattice simulations for heavy quarks (that are therefore static). This potential, shown in the figure 3, behaves as a standard  $1/r$  Coulomb potential at short distance, but increases linearly at large distance, in sharp contrast with electromagnetic interactions. This leads to *color confinement*, that is the fact that free color charges cannot exist in Nature. Quarks only appear in color singlet bound states called hadrons, made of 3 quarks (baryons) or quark-antiquark pairs (mesons). The spectrum of these bound states can in principle be determined from first principles from the QCD Lagrangian, and it depends only on the quark masses and on the QCD scale  $\Lambda_{QCD}$ . However, this dependence is non-perturbative and lattice simulations are the only way to perform these calculations. Presently, lattice calculations can reproduce the spectrum of light hadrons with an accuracy of the order of 5%, as illustrated in the figure 4.

The QCD running coupling shown in the figure 2 can also be viewed with a different perspective: it suggests that if one squeezes many hadrons in a small volume, then the average inter-quark distance will be small and their interactions

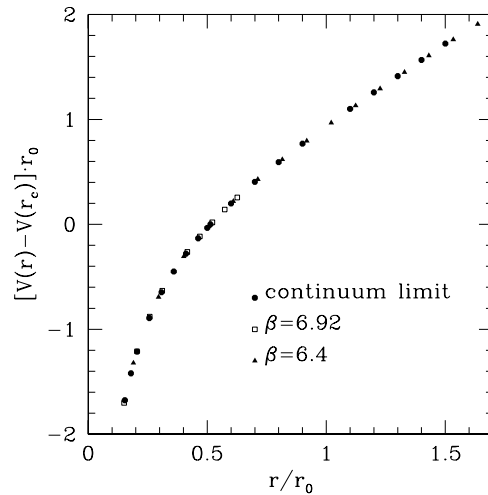


Fig. 3. Coulomb potential of a heavy quark and antiquark pair, from lattice QCD.

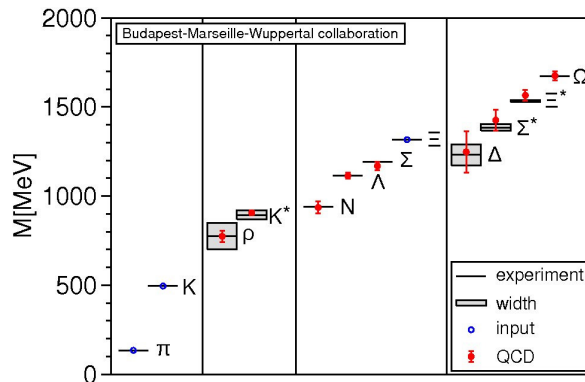


Fig. 4. Hadron spectrum from lattice QCD.

will be weak. In such a situation, the quarks would not be confined into individual hadrons, and would instead form a plasma made of deconfined quarks and gluons. This idea is substantiated by lattice calculations of the QCD partition function as a function of temperature, that indicate a rapid increase of the number of effective degrees of freedom at a temperature around 160 MeV<sup>b</sup>. This suggests that the relevant degrees of freedom are no longer the color singlet light hadrons (pions, kaons,...) and have been replaced by quarks and gluons (that are more numerous because of the uncovered color degree of freedom).

<sup>b</sup>This is for QCD with 3 light quark flavors. The transition temperature is higher for pure glue QCD.

## 2.2. Heavy ion collisions

Experimentally, the conditions of such a transition can be realized by colliding heavy nuclei at high energy. Such experiments are presently being performed by the RHIC (gold nuclei collided at 200 GeV) and by the LHC (lead nuclei collided at 5.5 TeV). Just after the impact of the two nuclei, the energy density reaches values that are more than ten times the normal nuclear matter density, well above the energy density at the deconfinement transition inferred from lattice calculations. Such a collision, whose total duration is of the order of 10 fm/c, can be divided into

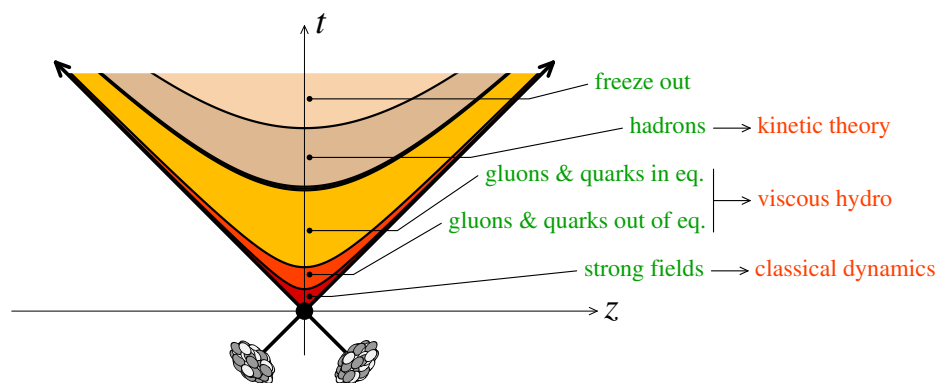


Fig. 5. Successive stages of a heavy ion collision.

several stages, as shown in the figure 5. In this figure, we have also indicated what kind of tool one may employ for each of these stages. It turns out that macroscopic descriptions such as relativistic hydrodynamics are quite successful at describing the bulk evolution of the system. Somewhat surprisingly, the matter produced in these collisions seems to behave almost like a perfect fluid with close to no viscosity. A very small viscosity suggests that this matter is not the siege of strong dissipative processes that would rearrange its microscopic degrees of freedom.

In these lectures, we will be primarily interested in the beginning of the collision, up to the point where a hydrodynamical description may become plausible. We will adopt a weak coupling perspective<sup>c</sup>, and we will try to follow a heavy ion collision in a description which is as close as possible to QCD. Indeed, in collisions at very high energy, the initial energy density is so large that the early stages of such a collision should be amenable to a weak coupling description, thanks to the asymptotic freedom of QCD. Note that a small viscosity, such that could explain the success of hydrodynamics, is more naturally obtained in the strong coupling limit because the viscosity is inversely proportional to the scattering cross-section of the quarks and gluons. However, it is also possible to get strong interactions

<sup>c</sup>In the discussion on gluon saturation, we will see that the emergence of the *saturation scale*, that increases with the collision energy, justifies this assumption.

at weak coupling, provided that the occupation number is inversely proportional to the coupling  $g^2$ . In this case, the coupling disappears from the scattering rate, and the system has many of the features of a strongly coupled system.

### 3. Parton model

#### 3.1. Kinematics

As discussed earlier, free quarks and gluons do not exist in normal nuclear matter. Instead they are confined into color singlet bound states, whose spectrum depends non-perturbatively on the parameters of the QCD Lagrangian. The same is true of the energy levels of a nucleus: they could in principle be derived from the underlying QCD dynamics, but this is even more complicated than in the case of light hadrons and at the moment far out of reach of lattice computations.

Does this mean that we should give up any hope of using QCD to describe collisions between such objects? Fortunately, the answer is no, *for collisions at sufficiently high energy*. The kinematics of these collisions is the key to overcome this difficulty. Let us consider first a nucleon at low energy (i.e. when the nucleon is almost at rest in the observer's frame), shown in the figure 6. In this cartoon, the

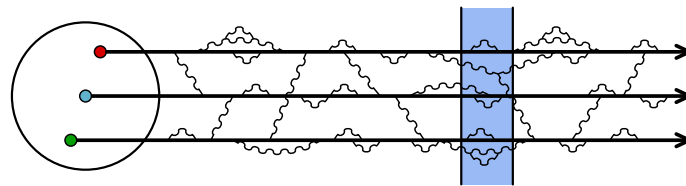


Fig. 6. Dynamics of the constituents inside a slow nucleon.

thick lines represent the three valence quarks, and the horizontal axis represents time. Only gluon constituents are shown, not the sea quarks. In such a frame, the valence quarks orbit with a period comparable to the proton size (they are ultrarelativistic). These quarks exchange gluons that provide the binding force, which also happens on scales of the order of the proton size. Moreover, the quarks and gluons can briefly fluctuate: for instance, a quark can temporarily become a quark+gluon state. The lifetime of these virtual states can be anything smaller than the proton size<sup>d</sup>. When studying reactions involving hadrons, one should compare the typical timescale of the collision (shown as a blue strip in the figure) with the timescales of the internal dynamics of the nucleon. In collisions involving low energy hadrons, the hadron has a complicated internal dynamics on timescales

<sup>d</sup>But since QCD is a renormalizable theory, the physics of the strong interactions at hadronic energy scales does not depend on what happens on much higher energy scales. Therefore, these short lived fluctuations have essentially no relevance in hadronic physics.

comparable to the duration of the collision, which makes these collisions untractable in perturbative QCD.

Contrast this with what happens in a collision at very high energy. Although scattering amplitudes are boost invariant and may be discussed in any frame, it is convenient to imagine that we do not change the momentum of one of the hadrons, and that all the energy increase is achieved by boosting the second hadron. This is illustrated in the figure 7. The blue strip, unchanged compared to the low energy case, may be viewed as the size of the first hadron, that we did not boost. All the changes are in the internal dynamics of the second hadron, whose timescales are now stretched by Lorentz time dilation. The gluon exchanges between the valence

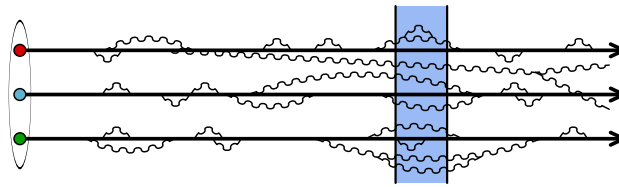


Fig. 7. Dynamics of the constituents inside a highly boosted nucleon.

quarks are now happening over timescales that are much longer than the duration of the collision, which means that the constituents of the nucleon can be viewed as free during the collision. The same happens to the fluctuations of the constituents. The lifetime of these virtual states is increased much beyond the collision timescales, making these off-shell constituents undistinguishable from on-shell particles<sup>e</sup>. Since there are fluctuations at arbitrary small timescales in a nucleon at rest, increasing the energy will uncover more and more of these fluctuations. These simple kinematical considerations are the essence of the *parton model*,<sup>9</sup> that approximates a high energy nucleon or nucleus as a collection of quasi-free constituents (called partons), whose density grows with energy.

### 3.2. Factorization

From this discussion, it seems that a QCD description of high energy collisions between hadrons may be feasible, provided we can provide “snapshots” of their partonic content at the time of the collision. What information is necessary in this snapshot is not completely obvious at this point, and may vary depending on the observable one intends to calculate, but for instance one may think of the following:

<sup>e</sup>The concept of on-shell or off-shell particles depends on the duration of the measurement. The only way to know that a particle is exactly on-shell is to perform an infinitely long measurement. Indeed, an off-shell particle may be viewed as a particle of momentum  $\mathbf{p}$  whose energy differs from the on-shell energy  $E_{\mathbf{p}}$  (given by the dispersion relation). A measurement that lasts  $\Delta t$  can only resolve energy differences of order  $1/\Delta t$  or larger.

- flavor and color of each parton,
- transverse position and longitudinal momentum.

Of course, these properties of a hadron cannot be known event by event, which means that at best a probabilistic description may be achieved, that would allow to compute expectation values for event averaged observables. However, the possibility of describing hadronic collisions with only a probabilistic partonic description of the incoming hadrons is highly non-trivial, because it is an approximation that amounts to discarding certain quantum interferences. Without doing any approximation, the transition probability from a pair of hadrons  $h_1 h_2$  to some final state  $X$  is obtained by summing all the relevant reaction channels before squaring the amplitude,

$$\begin{array}{l} \text{transition probability} \\ \text{from hadrons to } X \end{array} \equiv \left| \sum_{h_1 h_2 \rightarrow X} \text{Amplitudes} \right|^2.$$

In contrast, the parton model as described above approximates the transition probability as follows,

$$\begin{array}{l} \text{transition probability} \\ \text{from hadrons to } X \end{array} \approx \sum_{\substack{\text{partons} \\ \{q, g\}}} \text{probability to find} \\ \{q, g\} \text{ in } \{h_1, h_2\} \otimes \left| \sum_{\{q, g\} \rightarrow X} \text{Amplitudes} \right|^2$$

which is clearly not equivalent to the previous formula. This approximation is called *initial state factorization*. Roughly speaking, the physical motivation for such a factorization is that the neglected terms are interferences between a hard process that occurs on the timescale of the collision and a process internal to one of the projectiles, happening on much longer timescales. The vast separation in their timescales is what makes the corresponding interference small. At a more formal level, this factorization can be established in QCD, with various degrees of sophistication<sup>f</sup> depending on the observable.

### 3.3. Single parton distributions

The most developed framework for this type of factorization is the DGLAP formalism, in which one describes the incoming hadrons by *single parton distributions*. These distributions depend on the hadron and on the parton under consideration, on the fraction  $x$  of longitudinal momentum carried by the parton, and on a momentum scale  $Q$  that can be viewed as the inverse of the transverse spatial resolution with which the hadron is probed. In the figure 8, the single parton distributions of a proton, extracted from deep inelastic scattering data, are shown at a fixed resolution scale  $Q$ . Although these distributions are non perturbative and cannot

<sup>f</sup>The weakest of these *factorization theorems* are based on *leading log factorization*, where the two formulas are shown to be equivalent for an infinite series of terms of the form  $(\alpha_s \log(Q))^n$  (where  $Q$  is some hard scale), but not for terms of the form  $\alpha_s(\alpha_s \log(Q))^n$ . *Next-to-leading log factorization* extends the proof of this equivalence to include terms in  $\alpha_s(\alpha_s \log(Q))^n$ , and so on. *All-orders factorization theorems*<sup>10–12</sup> prove that the two formulas are equivalent up to terms that decrease as inverse powers of the hard scale.

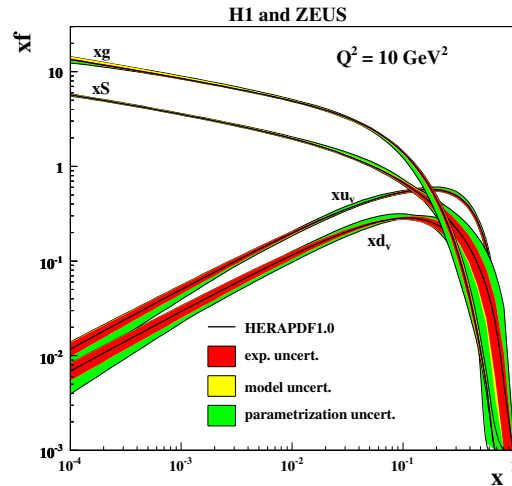


Fig. 8. Parton distributions of a proton, at the resolution scale  $Q^2 = 10 \text{ GeV}^2$ . From.<sup>13</sup>

be computed easily from the QCD Lagrangian<sup>8</sup>, QCD predicts how they change if one increases the resolution scale  $Q$ , via the *DGLAP equation*.<sup>14–17</sup> From this figure, one sees that the valence quark distribution is predominant at large values of the momentum fraction  $x \gtrsim 0.1$ , and is totally negligible at small  $x$ . At any value  $x \lesssim 0.1$ , the gluons are the dominant species of partons, and their density increases like a power of  $1/x$  when  $x \rightarrow 0$ . The sea quarks follow the trend set by the gluons, but with a suppression factor of order  $\alpha_s$  since they are produced by the process  $g \rightarrow q\bar{q}$ .

## 4. Gluon saturation

### 4.1. Dense regime of QCD

Since the DGLAP factorization framework is based solely on the single parton distributions, it is expected to become insufficient at large parton densities. The problem that will arise in this regime is illustrated in the figure 9, that shows side to side a typical scattering process in the dilute (left) and dense (right) regimes. In the dilute situation, the incoming hadrons are “mostly empty”, and hard scatterings are rare processes. Moreover, reactions involving more than one parton in each projectile are extremely rare (their rate scales as the square of the probability to find a parton). But when the parton density is large, processes initiated by multiple partons become

<sup>8</sup>Lattice QCD can be used to evaluate the first few Mellin moments of parton distributions, since they are given by expectation values of local operators that can be evaluated in the Euclidean theory.

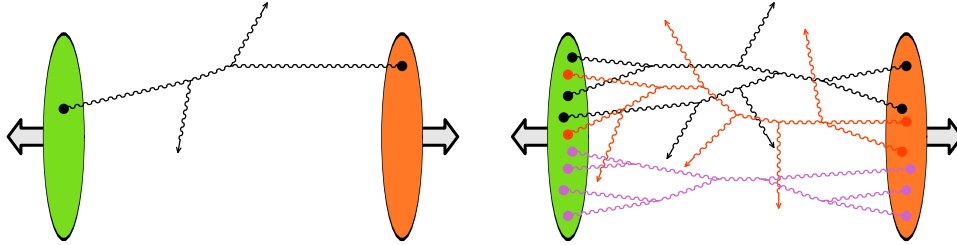


Fig. 9. Typical partonic processes in a collision between dilute (left) and dense (right) projectiles.

more likely to happen. Moreover, the partons that lie nearby in phase-space may be correlated, and therefore multiparton distributions cannot be inferred simply from single parton distributions. A framework that would enable one to calculate these processes should provide information about multiparton distributions in hadrons and nuclei, and thus should go beyond the DGLAP framework. Moreover, when the parton density becomes of the order of the inverse coupling  $1/g^2$ , a strongly interacting regime –called *gluon saturation*<sup>1–3</sup>– is reached, where an infinite series of Feynman graphs contribute at each order in  $g^2$ .

A hint of the fact that the small  $x$  saturation regime is qualitatively different from the dilute regime appears when plotting the deep inelastic scattering cross section slightly differently. This cross-section depends on two independent Lorentz invariant quantities,  $x$  and the 4-momentum squared  $Q^2$  of the photon exchanged in the scattering. However, when plotted against the combination  $x^{0.32}Q^2$ , this data appears to line up on a unique curve (see the figure 10). This scaling signals the

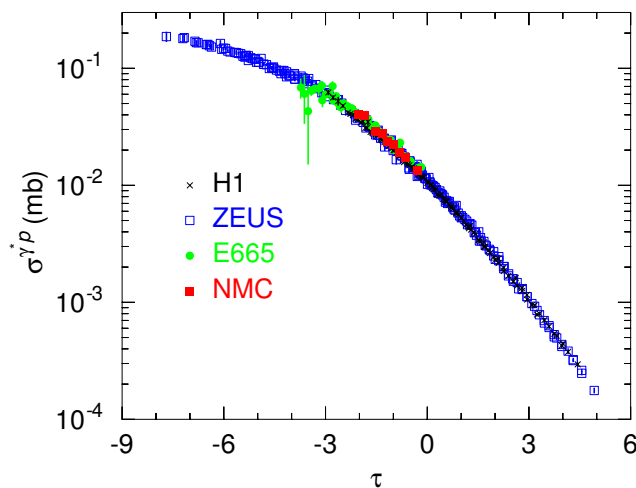


Fig. 10. Geometrical scaling in the DIS cross-section at small  $x$ . The horizontal axis represents the variable  $\tau \equiv x^{0.32}Q^2$ .

emergence of an  $x$  dependent momentum scale, that behaves roughly as  $Q_s^2(x) \sim x^{-0.32}$ . This scale, known as the *saturation momentum*, appears as a consequence of the nonlinear interactions among the gluons, that become important at high density.

#### 4.2. Saturation condition

To understand the onset of gluon saturation, it is instructive to go back to the dilute regime at large  $x$ . In this situation, a hadron appears as a loose collection of a few partons. When the hadron is progressively boosted, these partons radiate more gluons by bremsstrahlung<sup>h</sup>, as illustrated in the top panel of the figure 11. As long as the density remains low enough, these cascades of gluons develop independently and the evolution<sup>i</sup> of the hadron structure is governed by the linear *BFKL equation*.<sup>18,19</sup> Since these additional gluons are contained within the geometrical volume of the

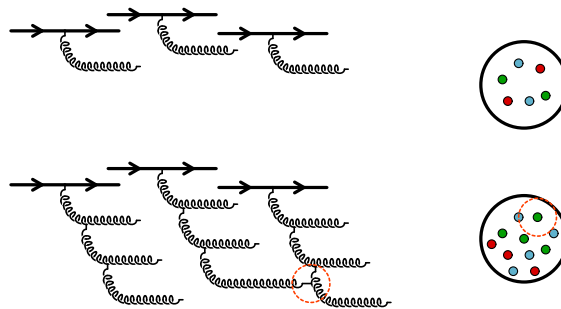


Fig. 11. Gluon cascades in the small  $x$  evolution of a hadron. Top: dilute regime. Bottom: onset of the recombination corrections.

hadron, their density increases rapidly. At some point, their wavefunctions start to overlap and their interactions are no longer negligible. Gluons from two different cascades can recombine, which tames the growth of the gluon density. Moreover, this recombination process makes the  $x$  evolution of the gluon distribution non-linear.

Before going into a more quantitative description of gluon saturation, it is easy to derive a simple criterion for the onset of saturation. Gluon recombination becomes likely when the product of the number of gluons per unit area with the cross-section for recombining two gluons into one becomes larger than one,

$$\underbrace{\alpha_s Q^{-2}}_{\sigma_{gg \rightarrow g}} \times \underbrace{A^{-2/3} x G(x, Q^2)}_{\text{surface density}} \geq 1 . \tag{4}$$

<sup>h</sup>As discussed before, these gluons are not truly on-shell, but can be viewed as real gluons if the lifetime of the quantum fluctuation that gave them birth is longer than the observation time.

<sup>i</sup>Although this terminology is commonly used, it is somewhat of a misnomer, since the hadron does not truly “evolve”. It is the observer’s view of the hadron content that changes as the observer’s frame is increasingly boosted with respect to the hadron.

This condition can be rearranged in order to obtain an inequality on  $Q$  :

$$Q^2 \leq \underbrace{Q_s^2}_{\text{saturation momentum}} \equiv \frac{\alpha_s x G(x, Q_s^2)}{A^{2/3}} \sim A^{1/3} x^{-0.3} . \tag{5}$$

This argument justifies the emergence of the saturation momentum, which characterizes the physics of gluon saturation. Saturation is important when the typical momentum scales in a process are smaller than  $Q_s$ . The region where this condition is satisfied is shown in the figure 12. From the more quantitative plot on the right panel of this figure, a typical value to keep in mind is that  $Q_s^2$  is in the range 2–4 GeV<sup>2</sup> for nuclei at the energy of the LHC. In the saturation domain,

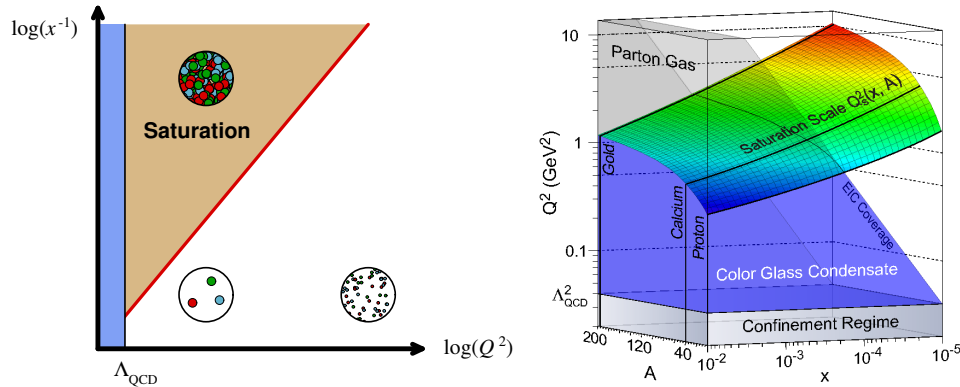


Fig. 12. Saturation domain in the  $x$  and  $Q$  plane. The 3-dimensional plot on the right adds information about the  $A$  dependence. From.<sup>20</sup>

non-linear gluon interactions are important, which arguably makes the calculation of such processes more complicated. However, this also has an unexpected positive side:  $Q_s$  now supersedes all the softer momentum scales in determining the typical momentum of the relevant partons, and thus also controls the running of the coupling. Since  $Q_s$  increases when  $x$  decreases (i.e. when going at higher energy), this opens an avenue for an ab initio weak coupling treatment of multiparton interactions (sometimes called the “underlying event” in other contexts) in high energy hadronic scatterings. From eq. (5), one sees that the saturation momentum also increases with the mass number of nuclei. This implies that, at a given energy, saturation effects are stronger in nucleus-nucleus collisions, for large nuclei<sup>j</sup>. This is important for heavy ion collisions at the RHIC and the LHC, because in these collisions the bulk of particle production is controlled by saturation physics.

<sup>j</sup>For gold or lead nuclei, the factor  $A^{1/3}$  that appears in  $Q_s^2$  is approximately 6.

## 5. Color Glass Condensate

### 5.1. Degrees of freedom

The Color Glass Condensate<sup>k</sup> (CGC) is a QCD based effective theory whose aim is to describe quantitatively the gluon saturation regime. The CGC exploits the high

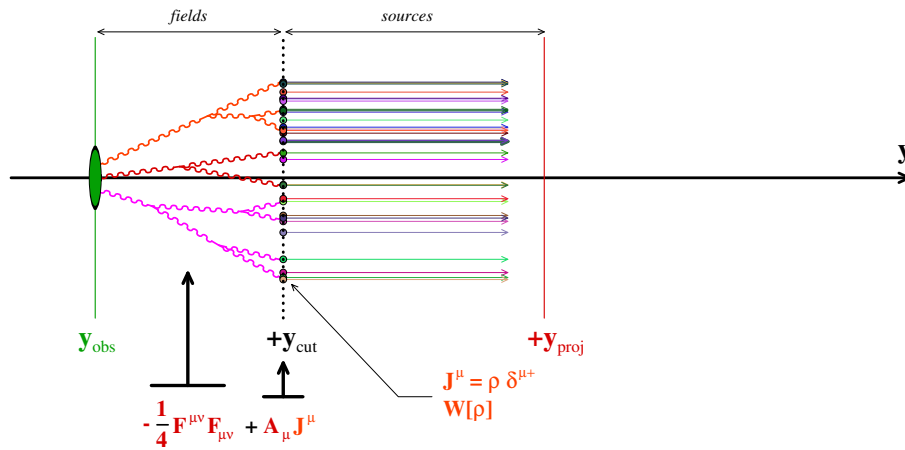


Fig. 13. Degrees of freedom in the CGC effective theory.

energy kinematics in order to simplify the description of the non-perturbative valence partons. The main idea was already encountered in the qualitative discussion of the parton model: a high energy hadronic collision is so brief that the fact that the partons are strongly bound by confinement is totally irrelevant. In fact, over such short timescales, the internal motion of the partons inside the hadron appears completely frozen. Thus, one may view the partons as static in the transverse plane, with a large longitudinal momentum.<sup>26–28</sup> For an observer sitting in the center of mass frame of the collision, the only information that matters about these partons is the color current  $J_a^\mu$  that they carry along the beam direction. The dominant component of this 4-vector is the longitudinal one. In light-cone coordinates, for a hadron moving in the  $+z$  direction, it reads

$$J_a^\mu(x) = \rho_a(x^-, \mathbf{x}_\perp) \delta^{\mu+}, \tag{6}$$

where the function  $\rho_a(x)$  is the density of color charges of the partons. It does not depend on the light-cone “time”  $x^+$  because of time dilation. Moreover, due to the concomitant Lorentz contraction, its  $x^-$  dependence is very peaked around  $x^- = 0$ .

It is important to realize that this drastic simplification cannot be used for all partons: it is applicable only to those partons whose longitudinal momentum (in the observer’s frame) is large enough. The partons that have a rapidity close to the

<sup>k</sup>For more detailed reviews of the Color Glass Condensate, one can consult Refs.<sup>21–25</sup>

observer's rapidity have comparable transverse and longitudinal momenta, and thus cannot be approximated by a longitudinal current. Moreover, for these partons, the Lorentz boost factor that slows down their time evolution is not large and one cannot neglect their dynamics. Therefore, these slower partons must be treated as full fledged quantum fields.

The situation is summarized in the figure 13: a cutoff  $y_{\text{cut}}$  must be introduced somewhere between the rapidity of the observer and the rapidity of the hadron under consideration. The partons close to the observer (mostly gluons, at least at leading order in  $\alpha_s$ ) are described as gauge fields, while those that are close to the projectile are approximated as a static longitudinal color current.

## 5.2. CGC effective theory

Thanks to the rapidity separation between the slow and the fast degrees of freedom in the CGC, their coupling can be treated as eikonal, i.e. via a term of the form  $J^\mu A_\mu$ . Therefore, the CGC can be summarized by the following effective action

$$\mathcal{S}_{\text{CGC}} = \int d^4x \left( -\frac{1}{4} F_{\mu\nu} F^{\mu\nu} + J^\mu A_\mu \right). \quad (7)$$

(For a collision of two hadrons, the current  $J^\mu$  is the sum of two terms, one for each hadron.) The function  $\rho_a(x^-, \mathbf{x}_\perp)$  that appears in the current  $J^\mu$  reflects the particular arrangement of the fast partons at the time of the collision. It is not a quantity that can be predicted event by event, and one can only have a statistical knowledge of this object. Therefore, the CGC also introduces a probability distribution  $W[\rho]$ . As we shall see later, all observable quantities must be averaged over all the possible configurations of  $\rho$ , according to the distribution  $W[\rho]$ ,

$$\langle \mathcal{O} \rangle = \int [D\rho] W[\rho] \mathcal{O}[\rho]. \quad (8)$$

In words, one should first calculate the observable for an arbitrary configuration of the color charge density  $\rho$  (in a collision of two hadrons, there is a  $\rho_1$  and a  $\rho_2$ ), and then perform a weighted average over all the possible  $\rho$ 's. The justification of this procedure will be given in the following two sections.

## 6. CGC at Leading Order

### 6.1. Power counting

So far, we have not assumed anything about the magnitude of the color charge density  $\rho_a$  that describes the fast partons in the CGC effective theory. For the CGC to be applicable to the saturated regime, we must allow  $\rho_a$  to be as large as the inverse coupling  $1/g$ . Indeed, the recombinations due to non-linear gluon interactions can stabilize the gluon occupation number at a value of order  $1/g^2$ , where the gluon splittings and the recombinations balance each other. Since the occupation number is quadratic in the gauge field, such a value corresponds to

$\rho \sim g^{-1}$ . As we shall see, such a large value of the source  $\rho$  simplifies the dynamics by making it classical at leading order, but complicates things by making an infinite set of graphs contribute at each order in  $g^2$ . In order to see this, let us first examine the power counting in the CGC effective theory. Consider a generic connected graph<sup>1</sup>, as shown in the figure 14. For such a graph, one finds that the order of

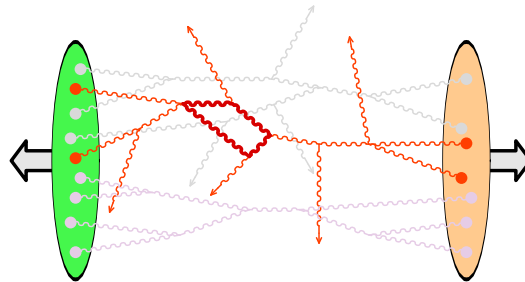


Fig. 14. Generic connected graph in the CGC effective theory. The dots represent the sources  $\rho$ . The lines terminated by arrows are the gluons produced in the final state.

magnitude depends only on the number of produced gluons and the number of loops, via the following formula<sup>29,30</sup>

$$\frac{1}{g^2} g^{\# \text{ produced gluons}} g^{2(\# \text{ loops})} . \tag{9}$$

The main consequence of assuming that  $\rho \sim g^{-1}$  is that this power counting does not depend on the number of sources that are included into the graph. The reason for this is that each additional source (of order  $g^{-1}$ ) is attached to the rest of the graph by a vertex (of order  $g$ ), and therefore does not contribute to the overall magnitude of the graph. This also means that, at each order in  $g^2$ , one must sum an infinite set of graphs.

For instance, the inclusive gluon spectrum has the following expansion in powers of  $g^2$

$$\frac{dN_1}{d^3\vec{p}} = \frac{1}{g^2} \left[ c_0 + c_1 g^2 + c_2 g^4 + \dots \right] , \tag{10}$$

where each of the coefficients  $c_0, c_1, \dots$  is itself an infinite series of terms of the form  $(g\rho)^n$ ,

$$c_i \equiv \sum_{n=0}^{\infty} c_{i,n} (g\rho_{1,2})^n . \tag{11}$$

At this point, we should make an important remark regarding exclusive versus inclusive observables. From the above power counting, we see that the average number of produced gluons in a high energy nucleus-nucleus collision is of order

<sup>1</sup>Typical graphs are not connected: they are made of many disconnected subgraphs. But it is sufficient to discuss the properties of one of these subgraphs.

$1/g^2$ . If we assume for simplicity that the multiplicity distribution is Poissonian<sup>m</sup>, the probability to have a given final state (e.g. a final state with a prescribed number of gluons) is exponentially suppressed by a factor  $\exp(-\#/g^2)$ . This factor may be viewed as a Sudakov factor that arises from excluding all the other final states. It turns out that these exclusive quantities are very difficult to calculate. In particular, the (disconnected) graphs that involve spectator partons contribute to exclusive observables, because these spectator partons may end up producing the unwanted final states.

In contrast, many simplifications occur in the calculation of inclusive quantities, that involve an average over all possible final states

$$\langle \mathcal{O} \rangle \equiv \sum_{\substack{\text{all final} \\ \text{states } f}} \mathcal{P}(AA \rightarrow f) \mathcal{O}[f]. \tag{12}$$

In particular, the high energy factorization results that will be discussed in the next section can only be established for these inclusive quantities, and their proof fails if one tries to generalize it to exclusive quantities.

### 6.2. Calculation of inclusive observables

The definition of eq. (12) suggests an elementary method for calculating inclusive quantities: compute the exclusive probabilities to end up in a given final state  $f$ , and sum over all possible  $f$ 's. However, it turns out that one can calculate them in a much more effective way without having to perform explicitly the sum over the final states. For this, one should use the *Schwinger-Keldysh formalism*,<sup>31,32</sup> in which this sum is already “built in”. Any contribution to eq. (12) is the product of an amplitude, a complex conjugate amplitude going to the same final state, and the observable evaluated on this final state, as illustrated in the figure 15. The

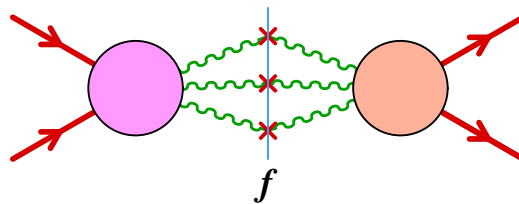


Fig. 15. Illustration of the Schwinger-Keldysh formalism.

diagrammatic rules for the amplitude (right of the dotted line) are the usual time-ordered Feynman rules. The propagator is the usual Feynman propagator, which for a (massless) scalar particle reads

$$G_{++}^0(p) = \frac{i}{p^2 + i\epsilon}. \tag{13}$$

<sup>m</sup>This is not exactly true in the CGC, but this fact does not change the essence of this argument.

For the complex conjugate amplitude (left of the dotted line), one needs the complex conjugate of the vertices and propagators. The propagator is therefore

$$G_{--}^0(p) = \frac{-i}{p^2 - i\epsilon}. \quad (14)$$

Across the dotted line, one must use special propagators that represent the on-shell particles of the final state  $f$ ,

$$G_{+-}^0(p) = 2\pi\theta(-p^0)\delta(p^2). \quad (15)$$

The Schwinger-Keldysh formalism amounts to the following:

- Draw all the graphs  $AA \rightarrow AA$  that have a given order in  $g^2$  (the power counting is the same as before, with each loop adding one power of  $g^2$ ).
- Sum over all the possibilities of assigning the labels  $+$  and  $-$  to the internal vertices.
- Only connected graphs contribute, because when summed over the  $+$  and  $-$  labels, the subgraphs that are not attached to the observable vanish.

These rules will automatically provide the sum over final states that was included in the formula (12). Note that when used in this context, the Schwinger-Keldysh formalism is equivalent to Cutkosky's cutting rules,<sup>33,34</sup> that were developed as a tool to compute the imaginary part of transition amplitudes. The superficial description of the Schwinger-Keldysh formalism that we have given here can be made more rigorous by writing the generating functional for its Green's functions. It can be obtained as follows from the generating functional  $Z[j]$  of time-ordered perturbation theory :

$$Z[j_+, j_-] = \exp \left[ \int d^4x d^4y G_{+-}^0(x, y) \square_x \square_y \frac{\delta^2}{\delta j_+(x) \delta j_-(y)} \right] Z[j_+] Z^*[j_-]. \quad (16)$$

This formula makes more obvious the fact that the Schwinger-Keldysh formalism is made of two copies of the ordinary Feynman perturbation theory (one of them complex conjugated), "stitched" together by the on-shell propagators  $G_{+-}^0$ .

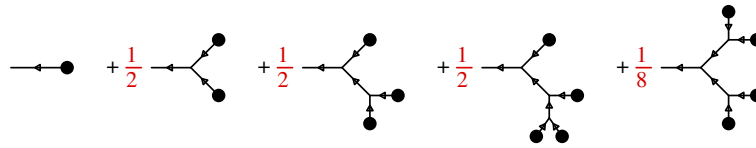
At this point, we have not really simplified the calculation of eq. (12). It has just been rephrased in a more systematic language. The simplifications come from noticing the following identities,

$$\begin{aligned} G_{++} + G_{--} &= G_{+-} + G_{-+} \\ G_{++} - G_{+-} &= G_{-+} - G_{--} = G_R \quad (\text{retarded propagator}). \end{aligned} \quad (17)$$

When using the Schwinger-Keldysh formalism to calculate inclusive observables at leading order, the sum over the  $+$  and  $-$  indices always generates the combinations of propagators that appear in the second of these equations, and these propagators therefore become retarded propagators.

### 6.3. Classical equation of motion

This simplification is particularly dramatic for inclusive observables at leading order. The starting point is a double sum over all possible tree diagrams (they all have the same order in  $g^2$  when the source is  $\rho \sim g^{-1}$ ) and over all the indices + and - of the Schwinger-Keldysh formalism. Thanks to the previous remark, the second sum merely replaces all the propagators by retarded propagators. One is thus left with a sum over all the tree diagrams built with retarded propagators, whose first few terms would be



(here for a  $\phi^3$  scalar field theory.) It is then easy to see that this sum is the solution of the classical field equations of motion that vanishes when  $x^0 \rightarrow -\infty$  (this retarded boundary condition follows from the fact that we are summing trees that are made of retarded propagators<sup>n</sup>). Although in interacting theories the classical equation of motion is a non-linear wave equation, this is a considerable simplification because we have now a problem that can be solved numerically.

The same simplifications work in the case of the CGC: at leading order, it is sufficient to solve the classical Yang-Mills equations with null retarded boundary conditions

$$[D_\mu, F^{\mu\nu}] = \rho_1 \delta^{\nu+} + \rho_2 \delta^{\nu-} \quad , \quad \lim_{x^0 \rightarrow -\infty} A^\mu(x) = 0 . \quad (18)$$

Assuming that we have solved this equation, all the inclusive observables at leading order can be expressed in terms of its solution  $\mathcal{A}^\mu$ . For instance, the single inclusive gluon spectrum is given by

$$\left. \frac{dN_1}{dY d^2\vec{p}_\perp} \right|_{\text{LO}} = \frac{1}{16\pi^3} \int_{x,y} e^{ip \cdot (x-y)} \square_x \square_y \sum_\lambda \epsilon_\lambda^\mu \epsilon_\lambda^\nu \mathcal{A}_\mu(x) \mathcal{A}_\nu(y) , \quad (19)$$

and the inclusive multigluon spectra simply read

$$\left. \frac{dN_n}{d^3\mathbf{p}_1 \cdots d^3\mathbf{p}_n} \right|_{\text{LO}} = \left. \frac{dN_1}{d^3\mathbf{p}_1} \right|_{\text{LO}} \times \cdots \times \left. \frac{dN_1}{d^3\mathbf{p}_n} \right|_{\text{LO}} . \quad (20)$$

Similarly, the components of the energy-momentum tensor have simple expressions in terms of the classical chromo-electric and chromo-magnetic fields  $\mathbf{E}^i$  and  $\mathbf{B}^i$ ,

$$T_{\text{LO}}^{00} = \frac{1}{2} [\mathbf{E}^2 + \mathbf{B}^2] \quad T_{\text{LO}}^{0i} = [\mathbf{E} \times \mathbf{B}]^i \quad (21)$$

$$T_{\text{LO}}^{ij} = \frac{\delta^{ij}}{2} [\mathbf{E}^2 + \mathbf{B}^2] - [\mathbf{E}^i \mathbf{E}^j + \mathbf{B}^i \mathbf{B}^j] . \quad (22)$$

<sup>n</sup>One can see here why it is important to consider inclusive observables for this simplification to happen. It is the sum over the final states that leads to the sum over the indices + and -. Without this sum, one would be left with time-ordered propagators, which would make the boundary conditions of the classical solution untractable.

#### 6.4. Numerical implementation

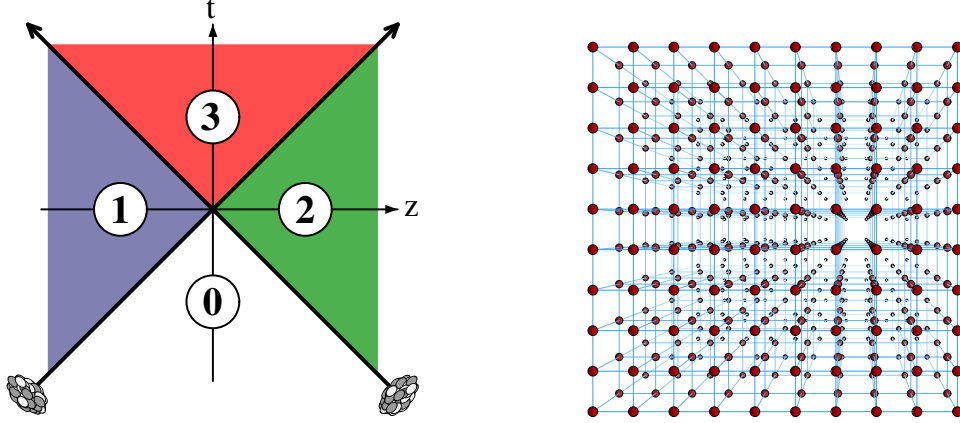


Fig. 16. Left: space-time structure of the classical gauge field  $\mathcal{A}^\mu$ . Right: 3-dimensional cubic lattice.

In order to perform this calculation in practice, one should be aware of the following :

- i. High energy collisions are nearly invariant under boosts in the longitudinal direction. This invariance has its simplest manifestation if one uses proper-time ( $\tau \equiv \sqrt{2x^+x^-}$ ) and rapidity ( $\eta \equiv \frac{1}{2} \log(x^+/x^-)$ ) as the coordinates inside the forward light-cone. When written in this system of coordinates, the classical Yang-Mills equations do not depend explicitly on rapidity, and thus become 1+2 dimensional equations.
- ii. The sources  $\rho_1$  and  $\rho_2$  have support on the light-cone, where they are singular, i.e. proportional respectively to  $\delta(x^-)$  and  $\delta(x^+)$ . These sources divide the space time in four distinct regions, as shown in the left figure 16. The gauge field is identically zero in the region 0, and it can be found analytically in the regions 1 and 2.<sup>35</sup> In the region 3, the best one can do analytically is to obtain the value of the gauge fields and the conjugate electrical fields just above the forward light-cone, at a proper time  $\tau = 0^+$ <sup>36</sup> :

$$\begin{aligned}
 A_0^i &= \alpha_1^i + \alpha_2^i \quad , \quad E_0^i = 0 \quad , \quad \alpha_n^i = \frac{i}{g} U_n^\dagger \partial^i U_n \quad (n = 1, 2) \quad , \\
 A_{0\eta} &= 0 \quad , \quad E_0^\eta = i \frac{g}{2} [\alpha_1^i, \alpha_2^i] \quad ,
 \end{aligned}
 \tag{23}$$

where the Wilson lines  $U_{1,2}(\mathbf{x}_\perp)$  read

$$U_1(\mathbf{x}_\perp) = \text{P} e^{ig \int dx^- \frac{-1}{\nabla_\perp^2} \rho_1(x^-, \mathbf{x}_\perp)} \quad .
 \tag{24}$$

Given these remarks, we need only to solve numerically 1+2-dimensional classical Yang-Mills equations inside the forward light-cone,<sup>37–46</sup> starting with the initial conditions (23). Choosing the time variable  $\tau$  determines the Hamiltonian of the system, and from there one can determine the Yang-Mills equations in Hamiltonian form. In order to handle them numerically, one must discretize space on a cubic lattice (see the right figure 16), while time remains a continuously varying variable. This is most easily done in the temporal gauge  $A^\tau = 0$  (also called the

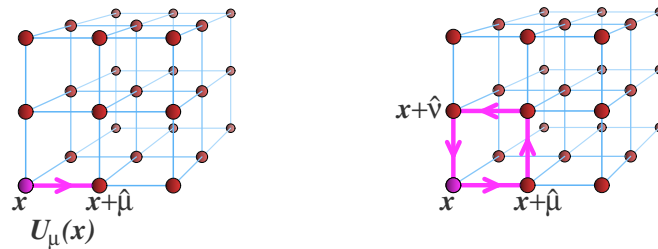


Fig. 17. Left: link variable. Right: elementary plaquette variable.

Fock-Schwinger gauge in this context). After having adopted this gauge condition, the problem has a residual gauge invariance, under any gauge transformation that depends only on space. Naive discretizations based on the gauge potentials  $A^\mu$  are not very adequate because they lead to violations of this residual gauge invariance. Instead, one should adopt Wilson’s formulation, in which the gauge potentials are traded in favor of link variables (see the left figure 17), i.e. Wilson lines that span one elementary edge of the lattice

$$U_i(x) \equiv \text{P exp } i g \int_x^{x+\hat{i}} ds A^i(s) . \tag{25}$$

Under a residual gauge transformation, these links transform as

$$U_i(x) \rightarrow \Omega(x) U_i(x) \Omega^\dagger(x + \hat{i}) . \tag{26}$$

The electrical fields  $E^i$  that appear in Hamilton’s equations transform covariantly,

$$E^i(x) \rightarrow \Omega(x) E^i(x) \Omega^\dagger(x) , \tag{27}$$

and therefore they should live on the nodes of the lattice. In the  $A^\tau = 0$  gauge, the Hamiltonian discretized in this fashion reads

$$\mathcal{H} = \sum_{\vec{x};i} \frac{E^i(\vec{x})E^i(\vec{x})}{2} - \frac{6}{g^2} \sum_{\vec{x};ij} 1 - \frac{1}{3} \text{Re Tr} ( \underbrace{U_i(x)U_j(x + \hat{i})U_i^\dagger(x + \hat{j})U_j^\dagger(x)}_{\text{plaquette at the point } \vec{x} \text{ in the } ij \text{ plane}} ) . \tag{28}$$

The only combinations of link variables that enter in this formula are *plaquettes* (i.e. the trace of the product of the four link variables that form an elementary

square on the cubic lattice), which are gauge invariant. The Hamilton equations that can be derived from this Hamiltonian form a large (but finite) set of ordinary differential equations, that can be solved numerically by standard methods such as the leapfrog algorithm.

### 6.5. Structure of the classical color fields

At very short times after the collisions ( $\tau \ll Q_s^{-1}$ ), the classical chromo-electric and chromo-magnetic fields are parallel to the collision axis,<sup>47</sup> as illustrated in the figure 18. By studying how the expectation value of transverse Wilson loops,<sup>48,49</sup>

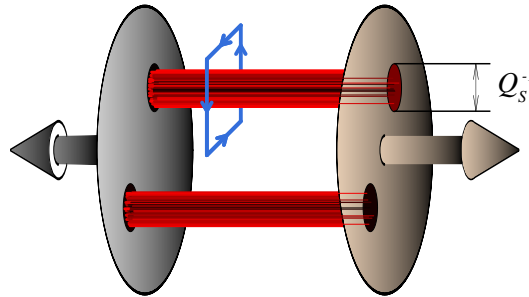


Fig. 18. Color flux tubes just after the collision.

$$W \equiv \left\langle \text{P exp } ig \int_{\gamma} dx^i \mathcal{A}^i \right\rangle, \quad (29)$$

depends on the area enclosed by the loop, one can infer the typical transverse size of these flux tubes. Indeed, one can roughly view the argument of the exponential as the magnetic flux going through the loop. It has been found that  $W$  decreases roughly as  $\exp(-\# \times \text{Area})$  for areas larger than  $Q_s^{-2}$ , which indicates that the fields are not correlated over transverse distances larger than  $Q_s^{-1}$ .  $Q_s^{-1}$  is therefore the typical radius of these flux tubes.

From the classical gauge fields, one can compute the spectrum of gluons produced in a heavy ion collision (see the figure 19). At large transverse momentum, the spectrum decreases as  $k_{\perp}^{-4}$ . Indeed, when  $k_{\perp} \gg Q_s$ , the saturation criterion is not satisfied and one should recover the usual perturbative results of the dilute regime. In contrast, saturation effects are quite large at small transverse momentum,  $k_{\perp} \lesssim Q_s$ , where they produce a strong softening of the spectrum, while the dilute result would still give a spectrum that grows as  $k_{\perp}^{-4}$  at small  $k_{\perp}$  (because there is no dimensionful scale other than  $k_{\perp}$  in the dilute calculation). Let us close this section by a remark concerning the energy dependence of the gluon multiplicity, obtained by integrating the gluon spectrum over  $k_{\perp}$ . The result is proportional to

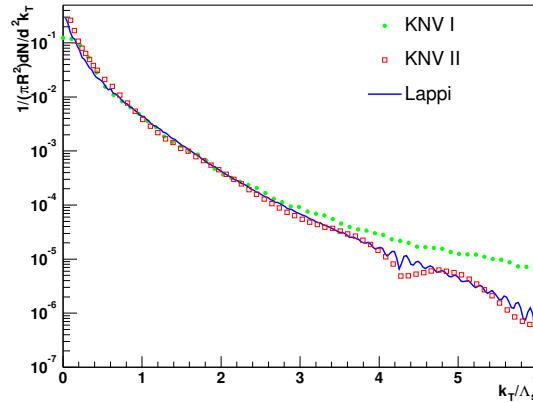


Fig. 19. Inclusive gluon spectrum.

the transverse area  $S_{\perp}$  multiplied by  $Q_s^2$ ,

$$N_{\text{gluon}} \sim \frac{S_{\perp} Q_s^2}{\alpha_s}. \quad (30)$$

From this pocket formula, one sees that the energy dependence of the gluon multiplicity is directly inherited from that of the saturation momentum,

$$N_{\text{gluon}} \sim x^{-0.3} \sim s^{0.15}. \quad (31)$$

Note that there is no contradiction between the fact that the multiplicity grows like a power of the collision energy and the Froissart bound, that tells us that hadronic cross-sections cannot grow faster than  $\sigma \sim \log^2(s)$ . The difference between the two is due to the fact that these two objects measure very different things. The total cross-section measures the probability that the two projectiles interact. As a probability, its growth is constrained by unitarity. In contrast, the gluon multiplicity measures the “amount of stuff” which is produced in a collision. It is not a probability, and is not bound by the same constraints. More precisely, the Froissart bound is related to the growth of the radius of the “black disk” region with energy (this radius grows like the log of energy). However, even after a certain region has become “black” (and thus its probability of interacting cannot grow anymore, because it has reached the unitarity limit), the number of gluons produced in this region will continue to grow like a power of energy (because the number of gluons per unit area in the incoming projectiles continues to increase like  $Q_s^2$ ).

## 7. Next to Leading Order

### 7.1. Improved power counting

From the power counting formula derived earlier, we expected for the gluon spectrum an expansion of the form

$$\frac{dN}{d^3\vec{p}} = \frac{1}{g^2} \left[ c_0 + c_1 g^2 + c_2 g^4 + \dots \right], \tag{32}$$

and we have seen in the previous section how to calculate the term  $c_0/g^2$ . The following terms,  $c_1, c_2 g^2, \dots$ , are given respectively by the sum of 1-loop, 2-loop, etc... diagrams. When calculating loops in the CGC framework, we have to recall that the degrees of freedom have been divided into sources and fields, separated by a cutoff  $y_{\text{cut}}$  in rapidity. In the integration over the loop momentum, we must use this cutoff in order to prevent the loop momentum to go into the kinematical domain which is described in terms of static sources. Failing to do this would lead to a double counting of the contribution of the modes that lie in this region.

In general, loop diagrams will depend on this cutoff:<sup>50</sup> a graph with  $n$  loops can contain up to  $n$  powers of  $y_{\text{cut}}$ . Therefore, the coefficients that appear in the  $g^2$  expansion of the gluon spectrum can themselves be expanded in powers of the cutoff as follows,

$$\begin{aligned} c_1 &= c_{10} + c_{11} y_{\text{cut}} \\ c_2 &= c_{20} + c_{21} y_{\text{cut}} + \underbrace{c_{22} y_{\text{cut}}^2}_{\text{Leading Log terms}} \end{aligned} \tag{33}$$

The terms that have the maximal degree in  $y_{\text{cut}}$ , i.e. a degree equal to the number of loops, are called the *leading log terms*<sup>o</sup>.

The cutoff  $y_{\text{cut}}$  was introduced by hand when defining the CGC, as a way of separating the two kinds of degrees of freedom, and it is therefore not a physical parameter. Observables should not depend upon it. As we shall see in this section, the leading log cutoff dependence that arises from loop corrections to observables can be absorbed into a redefinition of the probability distribution  $W[\rho]$ . This redefinition turns  $W[\rho]$  into a cutoff dependent object, but its cutoff dependence is universal, which means that the same distributions can be used for all inclusive observables.

Before we continue with a discussion of the leading log terms, let us also mention the fact that the next-to-leading log corrections are now known in some cases: in the BK equation (a mean field approximation of the JIMWLK equation)<sup>51-54</sup> and also for the JIMWLK equation.<sup>55-58</sup> The running coupling corrections have been used in some phenomenological studies<sup>59-63</sup> where they appear to be quantitatively important.

<sup>o</sup>The terminology comes from the fact that  $y_{\text{cut}}$  is the logarithm of a cutoff on the longitudinal momentum.

## 7.2. NLO result

Let us give here a sketch of the proof of this factorization. The first step is the derivation of an expression for the NLO correction to inclusive observables. It turns out that there exists a formal relationship between the LO and NLO contributions, valid for any inclusive observable, that reads:<sup>64,65</sup>

$$\mathcal{O}_{\text{NLO}} = \left[ \frac{1}{2} \int_{\mathbf{u}, \mathbf{v}} \mathbf{\Gamma}_2(\mathbf{u}, \mathbf{v}) \mathbb{T}_{\mathbf{u}} \mathbb{T}_{\mathbf{v}} + \int_{\mathbf{u}} \boldsymbol{\alpha}(\mathbf{u}) \mathbb{T}_{\mathbf{u}} \right] \mathcal{O}_{\text{LO}} . \quad (34)$$

In this formula, the LO observable  $\mathcal{O}_{\text{LO}}$  should be viewed as a functional of the initial value of the classical field on some space-like hypersurface (the integrations over the variables  $\mathbf{u}$  and  $\mathbf{v}$  are on this surface). The operator  $\mathbb{T}_{\mathbf{u}}$  is the generator of shifts of this initial condition, in the sense that its exponential translates the initial field  $\mathcal{A}_{\text{init}}$  in any quantity that can be expressed in terms of the classical field

$$\exp \left[ \int_{\mathbf{u}} \boldsymbol{\alpha}(\mathbf{u}) \mathbb{T}_{\mathbf{u}} \right] \mathcal{F}[\mathcal{A}_{\text{init}}] = \mathcal{F}[\mathcal{A}_{\text{init}} + \boldsymbol{\alpha}] . \quad (35)$$

The remarkable property of eq. (34) is that the coefficient functions  $\mathbf{\Gamma}_2$  and  $\boldsymbol{\alpha}$  are universal: they do not depend on the observable under consideration. Note however that although this formula is valid for all inclusive observables, it is not true for exclusive observables.

## 7.3. Classical phase-space formulation of quantum mechanics

In the formula (34), the operator between the square brackets acts only on the initial value of the classical fields, while the time evolution from the initial time surface to the time where the observable is evaluated remains classical. This is in fact a completely general result in quantum mechanics: at the first order in  $\hbar$ , the time evolution remains classical and  $\hbar$  enters only in the initial condition. Let us make a digression to justify this important point. This is best viewed if one rewrites the evolution equation for the density operator,

$$\frac{\partial \hat{\rho}_\tau}{\partial \tau} = i \hbar [\hat{H}, \hat{\rho}_\tau] , \quad (36)$$

in terms of the Wigner transforms of  $\hat{\rho}_\tau$  and  $\hat{H}$ ,

$$\begin{aligned} W_\tau(\mathbf{x}, \mathbf{p}) &\equiv \int d\mathbf{s} e^{i \frac{\mathbf{p} \cdot \mathbf{s}}{\hbar}} \langle \mathbf{x} + \frac{\mathbf{s}}{2} | \hat{\rho}_\tau | \mathbf{x} - \frac{\mathbf{s}}{2} \rangle \\ \mathcal{H}(\mathbf{x}, \mathbf{p}) &\equiv \int d\mathbf{s} e^{i \frac{\mathbf{p} \cdot \mathbf{s}}{\hbar}} \langle \mathbf{x} + \frac{\mathbf{s}}{2} | \hat{H} | \mathbf{x} - \frac{\mathbf{s}}{2} \rangle . \end{aligned} \quad (37)$$

(The Wigner transform of  $\hat{H}$  is nothing but the classical Hamiltonian of the system.) Note that in these Wigner transforms, the variables  $\mathbf{x}$  and  $\mathbf{p}$  are classical phase-space

variables, not operators. It is straightforward to show that eq. (36) is equivalent to

$$\begin{aligned} \frac{\partial W_\tau}{\partial \tau} &= \mathcal{H}(\mathbf{x}, \mathbf{p}) \frac{2}{i\hbar} \sin\left(\frac{i\hbar}{2} (\overleftarrow{\partial}_{\mathbf{p}} \overrightarrow{\partial}_{\mathbf{x}} - \overleftarrow{\partial}_{\mathbf{x}} \overrightarrow{\partial}_{\mathbf{p}})\right) W_\tau(\mathbf{x}, \mathbf{p}) \\ &= \underbrace{\{\mathcal{H}, W_\tau\}}_{\text{Poisson bracket}} + \mathcal{O}(\hbar^2). \end{aligned} \tag{38}$$

The first line is known as the *Moyal equation*. It is equivalent to the von Neumann equation for  $\hat{\rho}_\tau$ , except that it is expressed entirely in terms of classical phase-space variables. This equation makes the classical limit particularly transparent if one expands in powers of  $\hbar$  the operator that appears in its right hand side. As one can see immediately, its zeroth order in  $\hbar$  is the usual Poisson bracket. This means that at the order  $\hbar^0$ , one recovers classical Hamiltonian mechanics. A remarkable feature of the Moyal equation is that it has no term of order  $\hbar^1$ . This means that at NLO, the time evolution of the system remains purely classical. The only quantum effects at order  $\hbar^1$  come via the initial condition, through the fact that the support of the Wigner distribution of a quantum state must have an extension of at least  $\hbar$ . The first correction to the Moyal equation arises at the order  $\hbar^2$ , i.e. at NNLO. At this order, one gets quantum corrections both in the initial condition and in the time evolution itself. This discussion also indicates that a formula such as eq. (34), where only the initial conditions are altered, presumably does not exist beyond NLO.

#### 7.4. Cutoff dependence

Eq. (34) is very useful in order to extract the cutoff dependence in inclusive observables at NLO, because this cutoff dependence is already present in the operator that acts on  $\mathcal{O}_{\text{LO}}$ . If we keep only the terms that are linear in the cutoff, we have<sup>64–66</sup>

$$\frac{1}{2} \int_{\mathbf{u}, \mathbf{v}} \Gamma_2(\mathbf{u}, \mathbf{v}) \mathbb{T}_{\mathbf{u}} \mathbb{T}_{\mathbf{v}} + \int_{\mathbf{u}} \boldsymbol{\alpha}(\mathbf{u}) \mathbb{T}_{\mathbf{u}} = y_{\text{cut}}^+ \mathcal{H}_1 + y_{\text{cut}}^- \mathcal{H}_2. \tag{39}$$

In this equation,  $y_{\text{cut}}^+$  and  $y_{\text{cut}}^-$  are the cutoffs corresponding to the right and left moving nucleus respectively, and  $\mathcal{H}_{1,2}$  are operators known as the *JIMWLK Hamiltonians*<sup>P</sup> of the two nuclei,<sup>67–75</sup>

$$\mathcal{H} \equiv \frac{1}{2} \int_{\vec{\mathbf{x}}_\perp, \vec{\mathbf{y}}_\perp} \frac{\delta}{\delta \rho_a(\vec{\mathbf{x}}_\perp)} \chi_{ab}(\vec{\mathbf{x}}_\perp, \vec{\mathbf{y}}_\perp) \frac{\delta}{\delta \rho_b(\vec{\mathbf{y}}_\perp)}, \tag{40}$$

where

$$\begin{aligned} \chi_{ab}(\vec{\mathbf{x}}_\perp, \vec{\mathbf{y}}_\perp) &\equiv \frac{\alpha_s}{4\pi^3} \int d^2 \vec{\mathbf{z}}_\perp \frac{(\vec{\mathbf{x}}_\perp - \vec{\mathbf{z}}_\perp) \cdot (\vec{\mathbf{y}}_\perp - \vec{\mathbf{z}}_\perp)}{(\vec{\mathbf{x}}_\perp - \vec{\mathbf{z}}_\perp)^2 (\vec{\mathbf{y}}_\perp - \vec{\mathbf{z}}_\perp)^2} \\ &\times \left[ \left(1 - \tilde{U}^\dagger(\vec{\mathbf{x}}_\perp) \tilde{U}(\vec{\mathbf{z}}_\perp)\right) \left(1 - \tilde{U}^\dagger(\vec{\mathbf{z}}_\perp) \tilde{U}(\vec{\mathbf{y}}_\perp)\right) \right]_{ab}. \end{aligned} \tag{41}$$

In this equation,  $\tilde{U}$  is a Wilson line in the adjoint representation, constructed from the gauge field  $A^+$  such that  $\nabla_\perp^2 A^+ = -\rho$ .

<sup>P</sup>If one expands this Hamiltonian at small  $\rho$ , one can recover the BFKL equation.<sup>18,19</sup>

### 7.5. Factorization

The formula (39) has two important consequences:

- i. This formula is the *sum* of two terms corresponding to the two nuclei, but there is no cutoff dependent term mixing the two nuclei. This means that the cutoff dependent terms are intrinsic properties of the nuclei prior to their collision, and this is the reason why it is possible to eliminate them by redefining the distributions of the sources  $\rho_{1,2}$  of the two projectiles.
- ii. Since the operator in the square brackets in eq. (34) is the same for all inclusive observables, the cutoff dependence is equally universal. This is the reason why it will be possible to define cutoff dependent distributions  $W[\rho_{1,2}]$  such that they cancel the cutoff dependence of all observables.

The property **i**, about the absence of mixing of the cutoff dependence between the two nuclei, can be understood simply in terms of causality. This is illustrated in the figure 20. Indeed, the cutoff dependence arises from the phase-space integration of

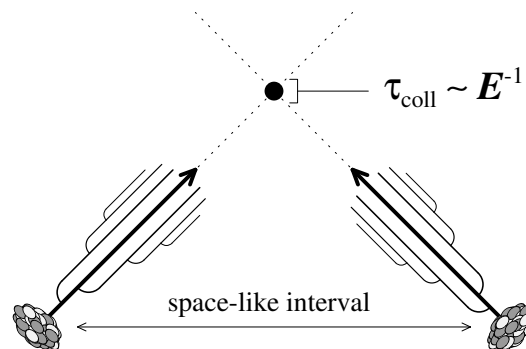


Fig. 20. Causality argument for factorization.

the soft gluons emitted by bremsstrahlung. Since they are soft, the formation time of these gluons is large: they cannot be emitted during the very brief duration of the collision, so they have to be emitted before the collision. Because the separation between the two nuclei is space-like until the collision, causality forbids any cutoff dependent term that would mix the two nuclei. The property **ii** also follows the same reasoning: gluon emissions that happen before the collision should be the same for all observables measured after the collision.

If we compute observables for fixed configurations  $\rho_1$  and  $\rho_2$  of the color charge densities in the two projectiles, there is no way to get rid of the cutoff dependence. The only way to remove it is to integrate over all the possible configurations of  $\rho_{1,2}$ . The main ingredient in this manipulation is the fact that the JIMWLK Hamiltonian

$\mathcal{H}$  is a self-adjoint operator:

$$\int [D\rho] W (\mathcal{H} \mathcal{O}) = \int [D\rho] (\mathcal{H} W) \mathcal{O}. \quad (42)$$

This property can be used to transfer the action of  $\mathcal{H}$  from the observable onto the distribution  $W[\rho]$ . From eq. (39), one can see that  $\rho$ -averaged quantities such as

$$\frac{dN_1}{d^3\vec{p}} \Big|_{\text{Leading Log}} = \int [D\rho_1 D\rho_2] W_1[\rho_1] W_2[\rho_2] \underbrace{\frac{dN_1}{d^3\vec{p}}}_{\text{fixed } \rho_{1,2}} \Big|_{\text{LO}} \quad (43)$$

are independent of the cutoff, provided that the distributions  $W[\rho]$  themselves depend on the cutoff according to the JIMWLK equation

$$\frac{\partial W}{\partial y} = \mathcal{H} W. \quad (44)$$

From eqs. (34) and (39), it is furthermore obvious that the same factorization formula (with the same  $W$ 's) applies to any inclusive observable.

In eq. (43), it is the evolution with rapidity of the distributions  $W$  that gives the gluon spectrum its rapidity dependence. Indeed, the gluon spectrum for fixed  $\rho_{1,2}$  that enters in the integrand is still independent of rapidity. From the JIMWLK equation, one sees that the distributions  $W$  evolve significantly for changes of the rapidity of the order of  $\Delta y \sim \alpha_s^{-1}$ . This factorization result thus predicts that the gluon spectrum is rather flat in rapidity at weak coupling.

### 7.6. Ridge correlations

Eq. (43) can be generalized to the inclusive multigluon spectrum. Recalling also eq. (20), we obtain the following factorization formula

$$\begin{aligned} \frac{dN_n}{d^3\vec{p}_1 \cdots d^3\vec{p}_n} \Big|_{\text{Leading Log}} &= \\ &= \int [D\rho_1 D\rho_2] W_1[\rho_1] W_2[\rho_2] \frac{dN_1}{d^3\vec{p}_1} \cdots \frac{dN_1}{d^3\vec{p}_n} \Big|_{\text{LO}}. \end{aligned} \quad (45)$$

This equation, valid at leading log accuracy, shows that at this order the correlations between the produced gluons only originate from correlations of the  $\rho$ 's of the incoming projectiles, since in the integrand the  $n$  gluons still appear completely factorized. Since the relevant rapidity interval for a significant JIMWLK evolution is  $\Delta y \sim \alpha_s^{-1}$ , this is also the typical rapidity distance over which the produced gluons will be correlated.

This is the basis of an interpretation of the peculiar shape of the 2-hadron correlations observed in heavy ion collisions. This correlation function is represented in the figure 21, as a function of the relative azimuthal angle and relative rapidity. As one can see, the correlation is very narrow in azimuthal angle, and very elongated

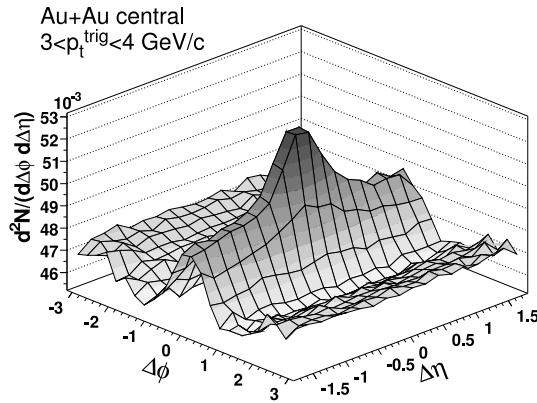


Fig. 21. Two hadron correlation measured in heavy ion collisions.<sup>76</sup>

in rapidity<sup>4</sup>. Because of causality, the existence of a correlation between particles that are widely separated in rapidity must originate from phenomena that happened very shortly after the collision. This is explained in the figure 22. Let us consider

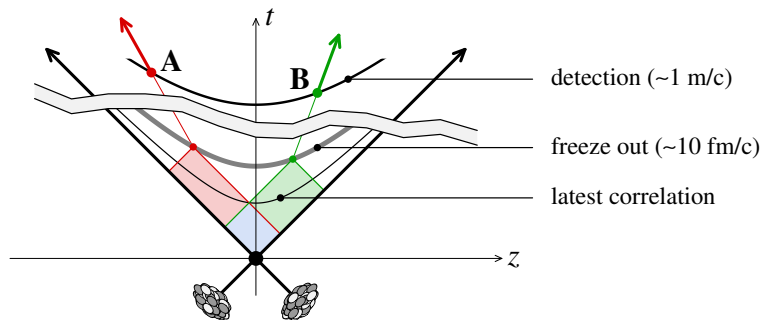


Fig. 22. Origin of the rapidity correlations.

the time evolution of two particles A and B in reverse, starting from their last interaction on the freeze-out surface. Obviously, by causality, they must come from the light-cones represented respectively in red and green in the figure. A correlation is an event that had an influence on both the particle A and the particle B. It must therefore have happened in the overlap between these two light-cones, that we have represented in blue. One sees clearly that there is a maximal time at which this correlation could possibly have been created. From the time of the freeze-out and the rapidity separation of the two particles, it is easy to determine this upper bound of the time,

$$\tau_{\text{correlation}} \leq \tau_{\text{freeze out}} e^{-|\Delta y|/2} . \tag{46}$$

<sup>4</sup>The peak in the middle is a jet-like correlation, due to quasi-collinear splittings in the final state.

This bound decreases very rapidly as one increases the rapidity separation  $\Delta y$ . In heavy ion collisions, the order of magnitude of the freeze-out time is 10 fm/c. For instance, a correlation between particles separated in rapidity by  $\Delta y = 6$  must be produced before the time 0.5 fm/c, which is well within the regime where the CGC is still applicable.

It is in fact easy to understand qualitatively the main features of the observed correlation from the structure of the classical color fields produced at early times in heavy ion collisions.<sup>77,78</sup> As we have said before, these fields are organized in flux tubes that have a typical transverse size of  $Q_s^{-1}$  and that remain coherent over rapidity intervals of order  $\alpha_s^{-1}$ . Two gluons emitted from the same tube are

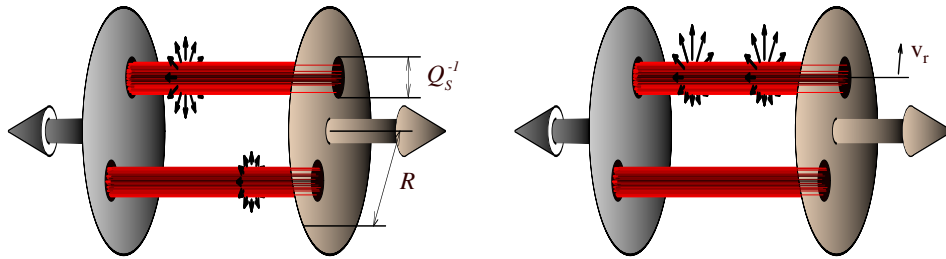


Fig. 23. Rapidity correlations from color flux tubes.

correlated if they are produced with a rapidity separation  $|\Delta y| \lesssim \alpha_s^{-1}$ , but are not correlated if they come from two different flux tubes<sup>r</sup>. From the size of the flux tubes, we conclude that the probability that two particles are correlated scales as  $(RQ_s)^{-2}$  where  $R$  is the transverse radius of the collision zone.

This explains the existence of a long range correlation in rapidity between pairs of particles, but not why their correlation is peaked in azimuthal angle. The 2-gluon correlation one gets from the CGC color fields is nearly independent of the azimuthal angle, because on average these gluons can be emitted in any transverse direction. However, one should keep in mind that the above causality argument applies only to the correlation in rapidity, not to the correlation in azimuthal angle that can be produced much later. These azimuthal correlations are generated by the radial flow<sup>79,80</sup> that develops subsequently and expels radially the matter produced in the collision. Simple relativistic kinematics indeed shows that if one boosts a 2-particle spectrum independent of azimuth, it becomes peaked around  $\Delta\phi = 0$  (the prominence of the peak increases with the velocity of the boost).<sup>77</sup> In the figure 24, we show a comparison of the strength of the azimuthal correlation in data and in a very basic radial boost model where a unique radial boost velocity is applied to a flat spectrum (the radial velocity is estimated from the slope of  $p_\perp$  spectra at

<sup>r</sup>The fact that the chromo-electric and chromo-magnetic fields are purely longitudinal at early time does not seem to play any role in this argument. The important properties are their coherence length in rapidity and in the transverse plane.

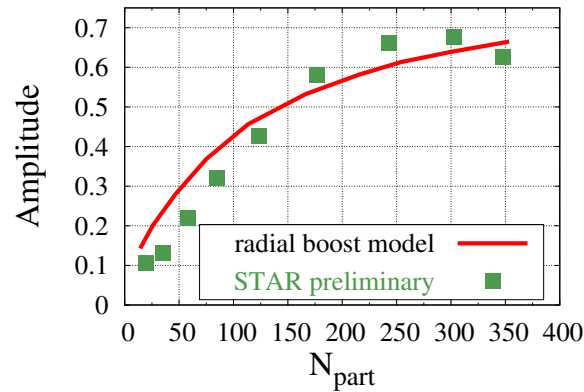


Fig. 24. Comparison of the strength of the azimuthal correlation in data and in a simple radial boost model<sup>81</sup> (see also<sup>82</sup>).

small momentum). The centrality dependence, which in this model comes from the increase of the radial velocity with centrality, is in fair qualitative agreement with the measurement.

## 8. From the Color Glass Condensate to hydrodynamics

### 8.1. Requirements for hydrodynamics

The CGC provides a self-contained QCD based framework for describing heavy ion collisions from first principles. It also provides tools for calculating inclusive observables at leading log accuracy, i.e. leading order plus a resummation of all the leading log contributions coming from higher loop diagrams. However, there is some physics that plays an important role in heavy ion collisions but is not easily captured in the CGC. The fact that the produced gluons and quarks will eventually hadronize when their energy density falls below the QCD critical energy density is obviously not present in the CGC (at least, at any fixed loop order).

For this reason, CGC calculations can only describe the early stages of the fireball expansion, and should be later on matched onto another description such as relativistic hydrodynamics.<sup>83–90</sup> Since the components of the energy momentum tensor can be computed in the CGC framework, one could use it as initial data for the hydrodynamical evolution. Firstly, for such a matching to be possible, the CGC must bring the system to a state that hydrodynamics can handle. This means that the transverse and longitudinal pressure should not be too different (in particular, the longitudinal pressure should not be negative), and that the viscous effects (e.g. the ratio  $\eta/s$  of the shear viscosity to the entropy density) should be small.

Moreover, when performing such a matching between two descriptions that use different degrees of freedom, one should be careful to check that the two descriptions

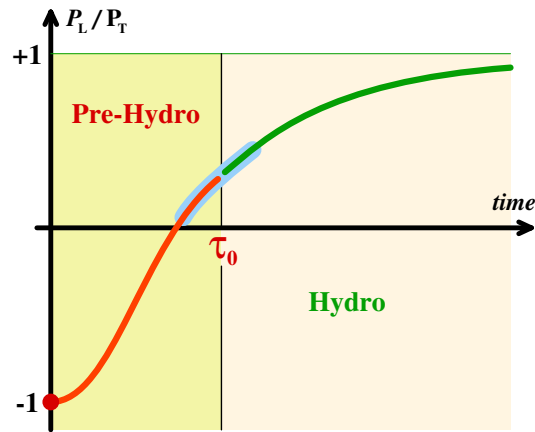


Fig. 25. Smooth matching between CGC and hydrodynamics.

are compatible in a certain time window. In other words, there should be some range where the two models predict equivalent results. If this is the case, the precise time  $\tau_0$  at which the matching is realized is not important, and it can be varied in this range without any incidence on the final result<sup>s</sup>.

The typical behavior of the ratio  $\eta/s$  in a gauge theory in equilibrium is shown in the figure 26. When the coupling is small, this ratio can be calculated in a weak

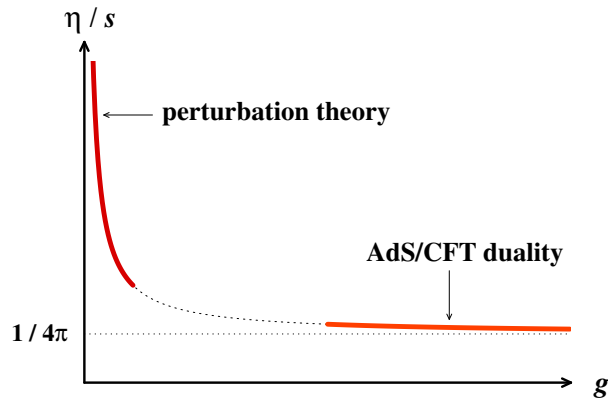


Fig. 26. Shear viscosity to entropy ratio in a gauge theory as a function of the coupling.

<sup>s</sup>This is very similar to the factorization of the source distribution  $W[\rho]$  in the calculation of inclusive observables. The independence with respect to the cutoff  $y_{cut}$  is possible because the static sources describe the same physics as the gauge fields in a certain range of longitudinal momentum.

coupling expansion. For QCD, it is given by

$$\frac{\eta}{s} \approx \frac{5.1}{g^4 \ln\left(\frac{2.4}{g}\right)}. \quad (47)$$

This formula shows that  $\eta/s$  is large at weak coupling. At large coupling, this quantity cannot be calculated in QCD, but there is an exact result for a supersymmetric cousin of QCD, the  $\mathcal{N} = 4$  SUSY Yang-Mills theory<sup>t</sup>:  $\eta/s = 1/(4\pi)$ .<sup>91,92</sup> From this plot, it seems that only strongly coupled systems can have a small  $\eta/s$  ratio. There is however another possibility to evade this conclusion. Firstly, one should recall the kinetic interpretation of the ratio  $\eta/s$ ,

$$\frac{\eta}{s} \sim \frac{\text{mean free path}}{\text{de Broglie wavelength}}. \quad (48)$$

In a system where the degrees of freedom have a typical momentum  $Q$ , the de Broglie wavelength is of order  $Q^{-1}$ , while the inverse mean free path is given by

$$(\text{mean free path})^{-1} \sim \underbrace{g^4 Q^{-2}}_{\text{cross section}} \times \underbrace{\int_{\mathbf{k}} f_{\mathbf{k}}}_{\text{density}} \underbrace{(1 + f_{\mathbf{k}})}_{\text{Bose enhancement}}. \quad (49)$$

The factor  $1 + f_{\mathbf{k}}$  under the integral is not needed when discussing dilute plasmas, but is important if the occupation number is large. In the CGC, just after the collision of two heavy ions, one has  $f_{\mathbf{k}} \sim g^{-2}$  up to  $k \sim Q$ . Therefore, in such a system one has  $\eta/s \sim g^0$ , which is much smaller than the perturbative result in equilibrium. It seems therefore plausible that the strong color fields produced in heavy ion collisions may flow, not because they are strongly coupled but because they are highly occupied.

## 8.2. Expansion and free streaming

The other main feature of heavy ion collisions is the very rapid expansion of the system in the longitudinal direction, which causes a redshifting of the longitudinal momenta. As illustrated in the figure 27, the pressure tensor tends to become anisotropic because of this, unless the interactions are strong enough to overcome the expansion. The figure shows what the expansion does on non-interacting particles. Starting from a nearly isotropic distribution of the velocities at the time  $\tau_1$ , the expansion will “filter out” the particles so that at the time  $\tau_2$  only particles with the momentum rapidity  $y \approx \eta$  exist at the space-time rapidity  $\eta$ . This means that, in the local comoving frame, the longitudinal pressure is much smaller than the transverse pressure. A large pressure anisotropy is a problem for hydrodynamics. Indeed, the difference between the longitudinal and transverse pressures goes into

<sup>t</sup>This gauge theory is conformal, and is dual to a string theory in an  $\text{AdS}_5 \times \text{S}_5$  background. The large coupling limit of the gauge theory corresponds to the weak coupling limit of the string theory, in which gravity becomes classical and reduces to Einstein’s equations.

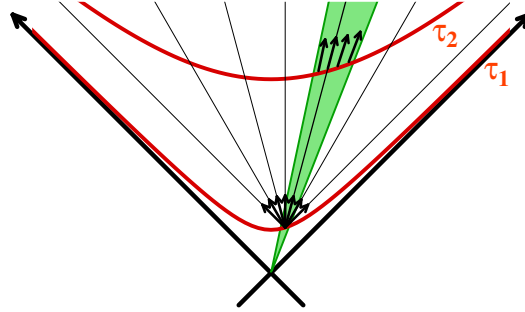


Fig. 27. Role of the expansion in decreasing the longitudinal pressure.

the viscous terms<sup>u</sup>, and large viscous corrections are a sign that hydrodynamics may incorrectly reproduce the underlying dynamics.

Let us now describe the CGC prediction for the energy momentum tensor, starting with the LO calculation<sup>v</sup>. Immediately after the collision, at  $\tau = 0^+$ , it is known analytically that the chromo-electric and chromo-magnetic fields are both parallel to the collision axis. This peculiar structure of the color fields implies that the energy momentum tensor is diagonal,  $T^{\mu\nu} = \text{diag}(\epsilon, P_T, P_T, P_L)$ , with<sup>w</sup>  $P_T = \epsilon$  and  $P_L = -\epsilon$ . At later times, the energy-momentum tensor must be determined numerically by solving the classical Yang-Mills equations, and by computing  $T^{\mu\nu}$  from the classical gauge fields according to eqs. (22). The results of this calculation<sup>47,100</sup> are shown in the figure 28. After starting at  $-1$ , the ratio  $P_L/\epsilon$  increases and becomes mostly positive at a time of order  $Q_s\tau \sim 1$ . However, this calculation shows that the longitudinal pressure remains at all times much smaller than the transverse one. Thus, the CGC at leading order leads to a situation which is similar to free streaming, where  $\epsilon, P_T \sim \tau^{-1}$  and  $P_L \ll \tau^{-1}$ . This leads to an unsatisfactory matching between the CGC at LO and hydrodynamics<sup>x</sup>, as illustrated in the figure 29. Indeed, in hydrodynamics the ratio  $P_L/P_T$  increases to approach 1 while it remains near zero in the CGC at LO.

<sup>u</sup>There are now attempts to view hydrodynamics as an expansion around a non-isotropic background. In this formulation, this may be less of a problem.<sup>93-99</sup>

<sup>v</sup>This discussion also applies to the LO result improved by the resummation of the leading log corrections. This does not change the conclusion of this paragraph since this resummation is totally absorbed into the rapidity evolution of the distributions  $W[\rho]$ .

<sup>w</sup>The negative longitudinal pressure in a longitudinal flux tube is the analogue of a string tension.

<sup>x</sup>In principle, this matching requires several steps: (1) compute  $T^{\mu\nu}(x)$  from CGC, (2) find its time-like eigenvector such that  $u_\mu T^{\mu\nu}(x) = \epsilon u^\nu$  (this defines the local rest frame, and the local energy density), (3) compute the pressure from some equation of state  $P = f(\epsilon)$ , (4) compute the viscous stress tensor as the difference between the full  $T^{\mu\nu}$  and the ideal part (obtained from  $\epsilon, P$  and  $u^\mu$ ). In many calculations using ‘‘CGC initial conditions’’, a simplified procedure is often employed, where one assumes that  $u^\mu = (1, \mathbf{0})$ : (1) compute  $\epsilon = T^{00}$ , (2) define  $P = f(\epsilon)$ , (3) neglect the viscous stress tensor.

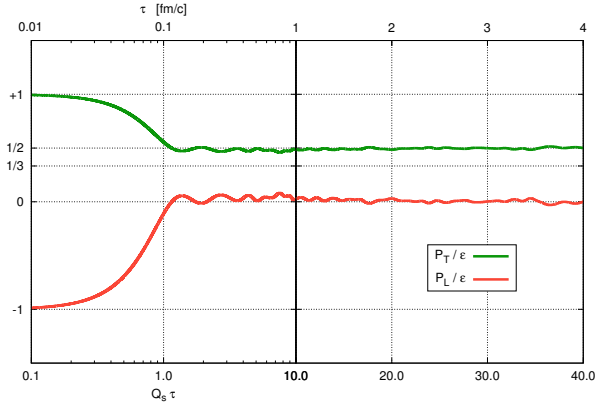


Fig. 28. Transverse and longitudinal pressure to energy density ratios, in the CGC at leading order.

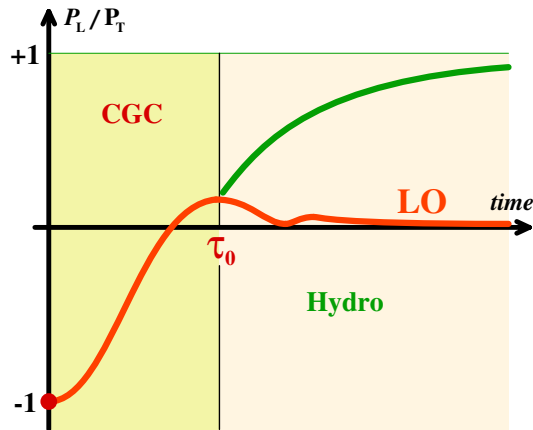


Fig. 29. Matching between hydrodynamics and the CGC at LO.

**8.3. A simpler model study case: thermalization in a box**

Before presenting recent works on isotropization and thermalization in heavy ion collisions, it is interesting to pause a brief moment on the same question for a hypothetical system of gluons enclosed in a fixed volume. In this case, the ultimate outcome is completely clear from the start: the system will eventually thermalize, and since its total energy is conserved one can predict from the start what will be the equilibrium temperature. The only issues are the timescale of the thermalization process, its possible dependence on the nature of the initial condition, and the shape of the gluon distribution at intermediate times before thermalization is complete.

A particularly interesting class of initial conditions are the so called “overoccupied” initial distributions, because they are also realized in heavy ion collisions in the CGC framework. The typical CGC-like initial condition has modes occupied up to the saturation momentum  $Q_s$ , with a large occupation number of order  $g^{-2}$ . It is called overoccupied because it contains too many particles for its energy density:

$$n \sim \frac{Q_s^3}{g^2} \quad , \quad \epsilon \sim \frac{Q_s^4}{g^2} \quad , \quad n\epsilon^{-3/4} \sim g^{-1/2} \gg 1 \quad , \quad (50)$$

while the dimensionless combination  $n\epsilon^{-3/4}$  should be of order 1 in a system with the same energy density in equilibrium. With such an initial condition, the mean free path in the system is parametrically shorter than the thermalization time, which leaves ample time for the system to forget its initial conditions long before reaching thermal equilibrium. With this type of initial condition, the hard scale of the system grows with time according to the following law<sup>101–103</sup>

$$\Lambda_H \sim Q_s (t/t_0)^{1/7} \quad , \quad (51)$$

and the distribution scales as

$$f(t, p) \sim (t_0/t)^{4/7} f(p/\Lambda_H) \quad . \quad (52)$$

The thermalization time can be estimated as the time at which the hard scale reaches the expected equilibrium temperature (i.e. the fourth root of the initial energy density),  $T_{\text{eq}} \sim Q_s g^{-1/2}$ . This gives a thermalization time that has the following parametric dependence on the coupling,

$$Q_s t_{\text{eq}} \sim g^{-7/2} \quad . \quad (53)$$

In a recent work<sup>104</sup> using the effective kinetic theory<sup>y</sup> of ref.,<sup>105</sup> this estimate was made more quantitative and the numerical prefactors computed to give

$$t_{\text{eq}} \approx \frac{72}{1 + 0.12 \log(\lambda^{-1})} \frac{1}{\lambda^2 T_{\text{eq}}} \quad , \quad (54)$$

where  $\lambda \equiv g^2 N_c$ .

This type of overoccupied initial condition has also led to speculations about the possibility of forming a Bose-Einstein condensate (BEC) in such systems, that would accommodate the excess of particles.<sup>102</sup> Such a condensate can only be transient, because the number of particles is not conserved in a relativistic quantum field theory. Therefore, the true equilibrium state cannot have a BEC. Whether such a condensate can form as a transient phenomenon depends on the magnitude of the initial overoccupation and the rate of the number changing processes. In a scalar  $\phi^4$  theory, where the rate of the inelastic processes is quite small compared to the elastic one, such a condensate has been observed in a number of numerical simulations.<sup>106,107</sup> The situation is much less clear in QCD, because the inelastic rate

<sup>y</sup>This effective theory includes  $2 \rightarrow 2$  processes dressed by in-medium masses, and effective  $1 \rightarrow 2$  and  $2 \rightarrow 1$  processes due to the quasi-collinear splitting of hard gluons by bremsstrahlung. For the latter, one must resum multiple scatterings, due to the Landau Pomeranchuk Migdal effect.

is enhanced by soft and collinear divergences. Unsurprisingly, kinetic theory calculations (based on a small scattering angle approximation of the matrix element) neglecting the inelastic processes do observe the formation of a BEC.<sup>108–110</sup> Extensions of these QCD kinetic theory computations to include inelastic processes<sup>111</sup> suggest that a BEC may still appear after including number changing processes, while other computations do not see any evidence for it.<sup>103,104</sup>

Note that for initially underoccupied<sup>2</sup> initial conditions, the evolution towards equilibrium is quite different. In particular, it is a lot less universal because the mean free path associated with the initial distribution is comparable to or longer than its value at equilibrium. In this situation, the initial hard particles first create a bath of soft particles by bremsstrahlung radiation, which thermalizes quickly. Then the remaining hard particles lose their energy by successive  $1 \rightarrow 2$  splittings induced by collisions on the soft background.

## 9. Weibel instability and resummation

### 9.1. Unstable classical solutions

There is however a good reason to explore the CGC beyond leading order: namely, the fact that the boost invariant solutions of the classical Yang-Mills equations are unstable.<sup>100,114–122</sup> When their initial condition is modified by a small but rapidity dependent perturbation, the solution diverges from the unperturbed one. This is illustrated in the figure 30, that shows a component of the energy momentum tensor that should be very small at all times if the perturbation was stable. Instead, it grows like an exponential<sup>a</sup>  $\exp \sqrt{\mu\tau}$  (the characteristic growth rate  $\mu$  is of the order of the saturation momentum  $Q_s$ ). These unstable modes in the classical Yang-Mills equations are closely related to the Weibel instability that occurs in anisotropic plasmas in QED and in QCD.<sup>101,113,123–142</sup> More details on how these instabilities of the classical solutions develop can also be found in refs.<sup>100,120,121,143</sup>

As we shall see in the next subsection, these instabilities are disastrous for the power counting that we have exposed earlier, where one keeps track only of the powers of  $g^2$ . Indeed, terms that have a higher order in  $g^2$  because they arise at a higher loop order may in fact contain time dependent factors that increase exponentially with time. These *secular divergences* mean that fixed loop order calculations are most likely unreliable (we will show an example of this in the next subsection), and that the power counting should be revisited and improved in order to capture the most important among those terms.

On the other hand, the existence of instabilities in the classical solutions of the

<sup>2</sup>In the bottom up scenario of ref.<sup>112</sup> (see also ref.<sup>113</sup>), it has been argued that in heavy ion collisions the expansion may turn a CGC-like initial condition into an underoccupied distribution before full thermalization is reached.

<sup>a</sup>The fact that  $\sqrt{\tau}$  appears here instead of  $\tau$  itself is due to the longitudinal expansion of the system. Because of the expansion, the equation that drives the growth of the perturbations is a Bessel equation instead of an ordinary wave equation.

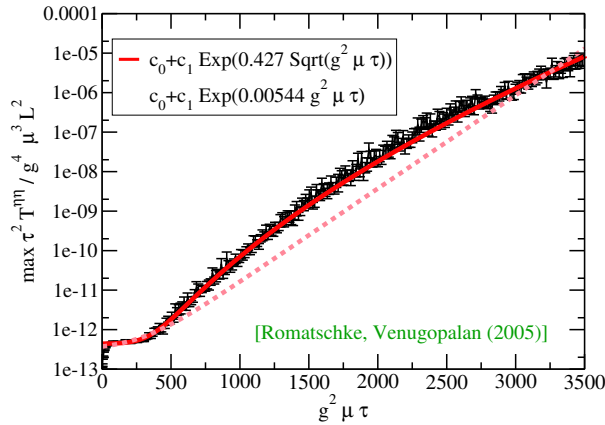


Fig. 30. Growth of unstable modes in classical Yang-Mills dynamics.

Yang-Mills equations may play a very important role in the statistical equilibration of the system. If we consider this system from the point of view of its classical phase-space, its initial condition at  $\tau = 0^+$  occupies a very compact region in phase-space. Indeed, at LO, the support of its Wigner distribution is a single point, since the LO is purely classical. At NLO, this support is broadened into a region of extension  $\hbar$ . If the dynamics was completely stable (as in an integrable system for instance, where the number of conservation laws equals the number of degrees of freedom), the size of this support would remain roughly constant in time, and at any subsequent time the system would still be far from statistical equilibrium. In contrast, an unstable dynamics will map this initially compact support into the extended portion of the phase-space allowed by the few conservation laws that remain valid. Measurements performed after such an evolution should bring results that are more in line with microcanonical equilibrium.

**9.2. Pathologies at fixed loop order**

These instabilities force us to reconsider the power counting that was the basis for organizing the expansion in powers of  $g^2$  of inclusive observables. As we have seen before, the one-loop corrections –that are formally of relative order  $g^2$ – contain leading log terms proportional to the cutoff  $y_{cut}$ , that can be absorbed into a redefinition of the distributions  $W[\rho]$ . Because of the instabilities, the 1-loop correction also contain some terms that grow exponentially in time. The best place to see this is via the following expression for the 2-point function  $\Gamma_2(\mathbf{u}, \mathbf{v})$  that enters in the formula (34),

$$\Gamma_2(\mathbf{u}, \mathbf{v}) = \int \frac{d^3 \mathbf{k}}{(2\pi)^3 2\omega_{\mathbf{k}}} a_{\mathbf{k}}(\tau_0, \mathbf{u}) a_{\mathbf{k}}^*(\tau_0, \mathbf{v}), \tag{55}$$

( $\tau_0$  is the initial time surface on which eq. (34) is expressed) where the functions  $a_{\mathbf{k}}(\tau, \mathbf{x})$  are small perturbations around the classical field encountered at leading order (for Yang-Mills theory, these functions would also carry color, spin and Lorentz indices not written explicitly in eq. (55)). They obey the equation

$$\left[ \mathcal{D}_\rho \mathcal{D}^\rho \delta_\mu^\nu - \mathcal{D}_\mu \mathcal{D}^\nu + ig \mathcal{F}_\mu{}^\nu \right] a_{\mathbf{k}}^\mu = 0$$

$$\lim_{x^0 \rightarrow -\infty} a_{\mathbf{k}}^\mu(x) = \epsilon^\mu(\mathbf{k}) e^{ik \cdot x}, \quad (56)$$

in which the covariant derivatives contain the LO classical field. The plane wave initial condition used in eq. (56) for these small perturbations can be understood from the explicit derivation of the formula (34).

The existence of instabilities means that, for some range of  $\mathbf{k}$ , the mode functions  $a_{\mathbf{k}}$  grow exponentially with time. The naive power counting derived so far implicitly assumed that the function  $\Gamma_2$  is of order  $g^0$ , but we never looked at its time dependence. From eq. (55), it is now obvious that it will become very large if some of the  $a_{\mathbf{k}}$ 's are unstable. Eventually, these exponential factors in  $\Gamma_2$  will compensate the  $g^2$  that comes from the loop, and these terms will be as large as the LO terms. This statement is illustrated in the figure 31, where we compare the

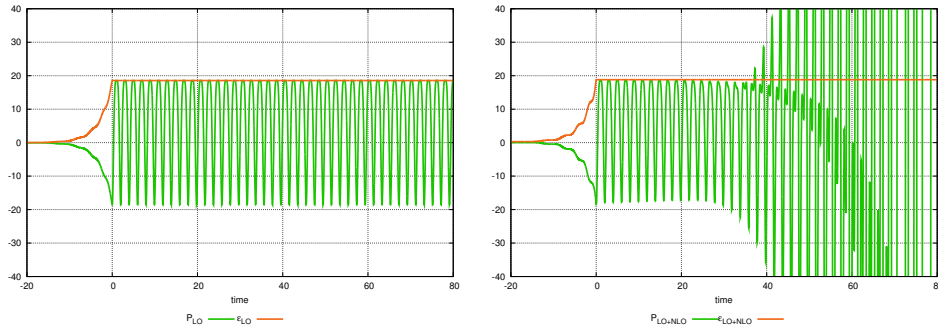


Fig. 31. Effect of parametric instabilities on the perturbative expansion of the energy-momentum tensor in a scalar  $\phi^4$  theory.

energy density and pressure at LO and LO+NLO in a  $\phi^4$  scalar field theory,<sup>144</sup> for which the solutions of the classical field equations of motion are also unstable<sup>b</sup>. This computation shows clearly that the fixed order LO+NLO result cannot be trusted after some time, because it becomes much larger than the LO result (note that this happens only for the pressure, because the energy density is protected from this exponential growth by energy conservation).

Although a similar NLO calculation has not been done in the CGC framework, one can guess what would happen. The Weibel instabilities would produce an

<sup>b</sup>The instability in the  $\phi^4$  theory is of a totally different nature, since it is caused by parametric resonance.<sup>145</sup> However, the detailed mechanism of the instability is not important in this discussion.

unbound growth of the longitudinal pressure, and this time the ratio  $P_L/P_T$  would be driven to arbitrarily large values exceeding unity. Attempting to match such a

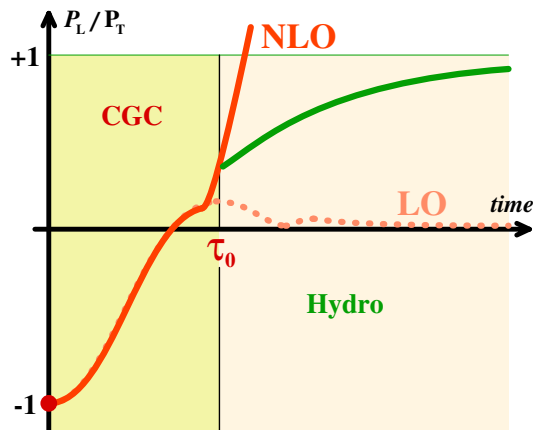


Fig. 32. Matching between hydrodynamics and the CGC at NLO.

NLO CGC initial condition to hydrodynamics would not be better than at LO, as illustrated in the figure 32.

### 9.3. Resummation of the leading terms

The same problem would in fact occur at any fixed loop order. The only way to improve the situation is to examine each loop order and to keep the most important terms at each order. For this, we need first to modify the power counting rules that we have established earlier, in order to keep track of the unstable modes. Let us first examine the graph that contributes at 1-loop, represented in the top-left corner of the figure 33, in conjunction with the formula (34). In this formula, each of the derivatives with respect to the initial classical field creates a perturbation to this classical field, that we have indicated by green propagators in the figure 33 (in the top-left graph, only the term proportional to  $\Gamma_2$ , that has second derivatives with respect to the initial fields, has been represented – the term with only one derivative has a slower growth with time). The “standard” power counting<sup>c</sup> would assign a factor 1 to  $\Gamma_2$  and a factor  $g$  to each of the derivatives  $\mathbb{T}_u$  (represented by a blue dot in the graphs). Thus the NLO correction to the energy-momentum tensor is expected to be of order  $g^0$ , while the LO is of order  $g^{-2}$ . From this diagrammatic representation, it is also easy to count the number of perturbations of the classical field. Each of them will develop into a factor of order  $\exp(\sqrt{\mu\tau})$  ( $\mu$  is of order  $Q_s$ ).

<sup>c</sup>For the term in  $\alpha\mathbb{T}$  in eq. (34), the standard counting has a factor  $g$  from  $\alpha$  and a factor  $g$  from the operator  $\mathbb{T}$ . However, we will not need to consider this term further since it has a subleading growth in time.

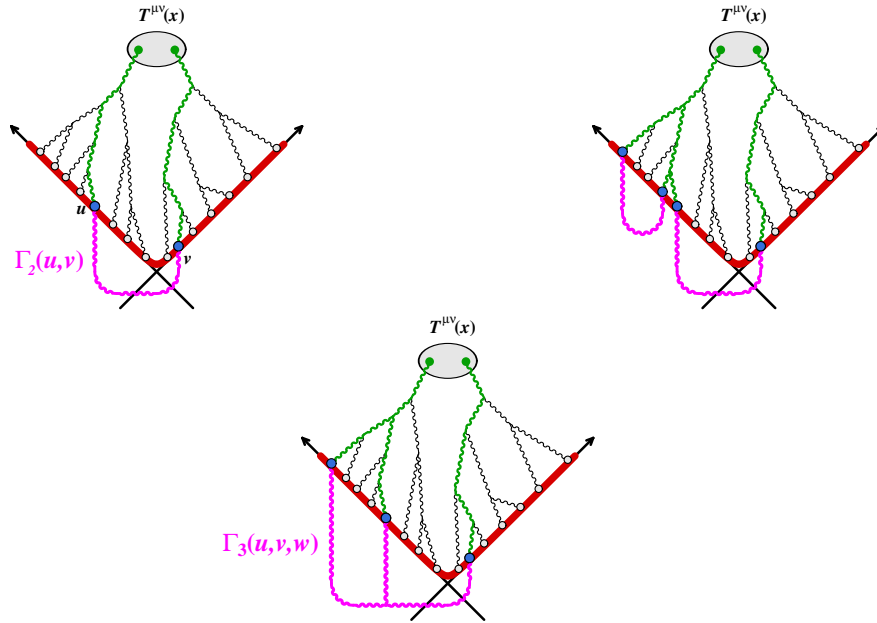


Fig. 33. Improved power counting taking into account the growth of the unstable modes.

Thus, the expansion of  $T^{\mu\nu}$  is more accurately written<sup>d</sup> as :

$$T^{\mu\nu} = c_0 g^{-2} + c_1 g^0 e^{2\sqrt{\mu\tau}} + \dots, \tag{57}$$

where the coefficients  $c_0, c_1$  do not grow exponentially with time. From this pocket formula, one can deduce at which time the naive loop expansion breaks down. This is the time when the one-loop result becomes as large as the leading order, i.e.

$$\tau_{\max} \sim \mu^{-1} \log^2(1/g^2). \tag{58}$$

Up to a logarithmic factor, this time is of the order of the inverse saturation momentum.

At two loops, the naive power counting tells us that we should get terms of order  $g^2$  (i.e.  $g^4$  relative to the leading order). However, not all the terms have the same growth in time. In the figure 33, we have represented two types of 2-loop contributions, in order to illustrate these differences. In the top-right graph, the two loops are the seed of four perturbations to the classical field, while in the bottom graph, only three of these perturbations are created. The latter term will therefore have a subleading behavior in time. Moreover, one sees that the distinguishing feature of the top-right graph is that it can be generated by acting twice with the

<sup>d</sup>This formula indicates the worst possible behavior. It is possible that some components of the energy-momentum tensor will not be affected by the instability, as was the case in the scalar field theory considered in the figure 31.

quadratic part of the operator that appears in eq. (34). This reasoning extends to all orders. At the  $n$ -th loop order, the maximal number of field perturbations that can be seeded on the light-cone is  $2n$ , and the corresponding graphs are generated by acting  $n$  times with this quadratic operator. The sum of all these leading terms can be obtained by

$$T_{\text{resummed}}^{\mu\nu} \equiv \exp \left[ \frac{1}{2} \int_{\mathbf{u}, \mathbf{v}} \Gamma_2(\mathbf{u}, \mathbf{v}) \mathbb{T}_{\mathbf{u}} \mathbb{T}_{\mathbf{v}} \right] T_{\text{LO}}^{\mu\nu}. \tag{59}$$

Note that the Taylor coefficients of the exponential correspond precisely to the symmetry factors of graphs such as the top-right diagram of the figure 33 (the  $1/2!$  of the second Taylor coefficient gives the symmetry factor that corresponds to the freedom of swapping the two  $\Gamma_2$ 's that are hanging below the light cone).

Moreover, if the 2-point function  $\Gamma_2$  used in eq. (59) is precisely the one that enters in the NLO result (34), then one has

$$T_{\text{resummed}}^{\mu\nu} = T_{\text{LO}}^{\mu\nu} + T_{\text{NLO}}^{\mu\nu} + \dots \tag{60}$$

In other words, this resummation contains the exact LO and NLO contributions, and a subset of all the higher loop contributions. It is important to keep in mind that, starting at the 2-loop order, it is an approximation which is not equivalent to the complete underlying theory. This will have important consequences that we will discuss later.

## 10. Classical statistical approximation (CSA)

### 10.1. Reformulation as a Gaussian average

At this point, the resummation performed via the eq. (59) is quite formal. Three questions must be addressed: (1) can this formula in terms of functional derivatives be evaluated in a practical way? (2) does eq. (59) lead to results whose time dependence is bounded? (3) when doing this, are we introducing other pathologies?

In order to answer the first question, one should recall the following identity:

$$e^{\frac{\alpha}{2} \partial_x^2} f(x) = \int_{-\infty}^{+\infty} dz \frac{e^{-z^2/2\alpha}}{\sqrt{2\pi\alpha}} f(x+z). \tag{61}$$

This formula can be established e.g. by applying a Fourier transform to both sides. Although we cast it here in a space of functions of a single variable, this formula can be generalized to operators that are Gaussian in derivatives over a functional space. It enables us to rewrite eq. (59) as<sup>e</sup>

$$T_{\text{resummed}}^{\mu\nu} = \int [Da] \exp \left[ -\frac{1}{2} \int_{\mathbf{u}, \mathbf{v}} a(\mathbf{u}) \Gamma_2^{-1}(\mathbf{u}, \mathbf{v}) a(\mathbf{v}) \right] T_{\text{LO}}^{\mu\nu} [\mathcal{A}_{\text{init}} + a]. \tag{62}$$

<sup>e</sup>Such a Gaussian averaging procedure has also been reached in other approaches.<sup>146-150</sup>

This resummation procedure, where one averages classical trajectories over an ensemble of initial conditions, is known as the *Classical Statistical Approximation* (CSA).

From this equation, one can easily see that the problem of the unbounded growth of the fluctuations has been cured. Indeed, this resummation has promoted the linearized perturbations<sup>f</sup> that appear in the NLO contribution into an integral part of the non-linear classical field (the initial condition of the classical field is modified by the perturbation, but its evolution remains fully non-linear). In any theory where the potential prevents the fields from running away to infinity, this guarantees that the resummed quantity will not diverge in time.

## 10.2. Practical implementation

In the form of eq (62), the procedure for evaluating the resummed energy-momentum tensor<sup>g</sup> is quite straightforward:

1. Determine the 2-point function  $\Gamma_2(\mathbf{u}, \mathbf{v})$  that defines the Gaussian fluctuations, for the initial time  $Q_s\tau_0$  of interest. This is an initial value problem, whose outcome is uniquely determined by the state of the system at  $x^0 = -\infty$ , and depends on the history of the system from  $x^0 = -\infty$  to  $\tau = \tau_0$ . This problem is solvable analytically as long as the fluctuations remain weak,  $a^\mu \ll Q_s/g$ . If they grow larger, the fluctuations start to interact non-linearly, and their spectrum becomes non-Gaussian. To avoid this, the initial time should be chosen such that  $Q_s\tau_0 \ll 1$ .
2. Solve the classical Yang-Mills equations from  $\tau_0$  to  $\tau_f$ . In high energy collisions, the problem as a whole is boost invariant, but individual field configurations are now rapidity dependent because of the fluctuating part superimposed to their initial condition. Therefore, unlike in the CGC at LO, the classical Yang-Mills equations must now be solved in 3+1 dimensions.
3. Do a Monte-Carlo sampling of the fluctuating initial conditions.

The setup for doing this is the same as the one described when discussing the CGC at LO, except for the fact that one must keep rapidity explicitly. One must discretize the classical Yang-Mills equations in the system of coordinates  $\tau, \eta, \mathbf{x}_\perp$ . The lattice used in these computations usually represents a sub-volume of the interaction region that expands in the longitudinal direction, as illustrated in the figure 34. This implies that the lattice spacing in the  $z$  coordinate is time dependent. In order to be able to resolve the physically relevant scales at the final time  $\tau_f$  of the simulation, it is usually necessary to have a larger number of lattice spacings in the

<sup>f</sup>One would recover the pathological behavior of the NLO result by linearizing the equation of motion for the classical field of initial condition  $\mathcal{A}_{\text{init}} + a$ .

<sup>g</sup>Although the discussion here is centered on the energy-momentum tensor, the same resummation can be applied to any inclusive quantity.

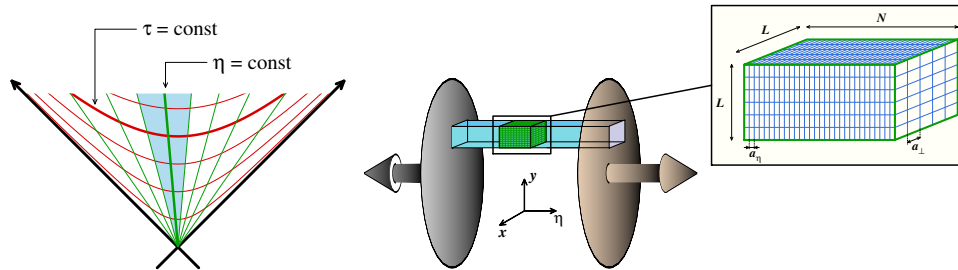


Fig. 34. Lattice setup for numerical implementations of the classical statistical method.

longitudinal direction.

### 10.3. CSA in quantum mechanics

The Classical Statistical Approximation has an analogue in ordinary quantum mechanics, which is helpful to understand what approximation is being made when one uses it. The starting point is the transformation that goes from the von Neumann equation (36) for the density operator to the Moyal equation (38) for its Wigner transform. The Moyal equation is still an exact representation of the quantum evolution of the system, although it is expressed in terms of objects that depend on classical phase-space variables. However, we have seen that if one expands the operator in the right hand side of eq. (38) to lowest order in  $\hbar$ , one recovers the classical Poisson bracket. In this approximation, the evolution of the system is thus purely classical. Note however that the initial condition can remain fully quantum in this approximation. For instance, if the system is initially in a pure quantum state  $|\psi\rangle$ , its initial Wigner distribution would be

$$W_0(\mathbf{x}, \mathbf{p}) \equiv \int d^3\mathbf{r} e^{i\mathbf{p}\cdot\mathbf{r}} \langle \mathbf{x} + \frac{\mathbf{r}}{2} | \psi \rangle \langle \psi | \mathbf{x} - \frac{\mathbf{r}}{2} \rangle = \int d^3\mathbf{r} e^{i\mathbf{p}\cdot\mathbf{r}} \psi^*(\mathbf{x} + \frac{\mathbf{r}}{2}) \psi(\mathbf{x} - \frac{\mathbf{r}}{2}). \tag{63}$$

If the initial state  $|\psi\rangle$  is known, then no approximation is needed in the CSA for the initial Wigner distribution. In this analogy, the Gaussian initial Wigner distribution that we have obtained in the previous subsection would correspond to starting from a coherent state, i.e. a state whose Wigner distribution is a Gaussian of width  $\hbar$  centered on some classical configuration.

### 10.4. CSA from the path integral

It is also instructive to see how the CSA can be derived from the path integral formulation of quantum field theory. Since we aim at calculating the expectation value of observables in a system initialized in a known state, we must use the

Schwinger-Keldysh formalism

$$\langle \mathcal{O} \rangle = \int [D\varphi_{\pm}^{(i)}(\mathbf{x})] \rho_0(\varphi_+^{(i)}, \varphi_-^{(i)}) \int [D\phi_{\pm}(x)] e^{iS[\phi_+] - iS[\phi_-]} \mathcal{O}(\phi), \quad (64)$$

where the field is doubled into a + component (that represents the evolution in the amplitude) and a – component (that describes the conjugate amplitude). In this formulation, the initial state of the system is represented by a density operator  $\hat{\rho}_0$ , whose matrix elements  $\rho_0(\varphi_+^{(i)}, \varphi_-^{(i)})$  control the distribution of the initial values of the fields  $\phi_{\pm}$ . The second integral is restricted to fields whose boundary value at the initial time is

$$\phi_{\pm}(t_0, \mathbf{x}) = \varphi_{\pm}^{(i)}(\mathbf{x}). \quad (65)$$

Inclusive observables do not put any constraint on the final state, and therefore the fields have no specific boundary condition at  $t = +\infty$  in the above path integral, except  $\phi_+ = \phi_-$  when the measurement is done.

From eq. (64), one should define new fields as the sum and difference of  $\phi_+$  and  $\phi_-$ ,

$$\phi_2 \equiv \frac{\phi_+ + \phi_-}{2}, \quad \phi_1 \equiv \phi_+ - \phi_-. \quad (66)$$

The difference  $S[\phi_+] - S[\phi_-]$  is obviously odd in the field  $\phi_1$ , and it is trivial to verify that the term linear in  $\phi_1$  comes as a prefactor of the classical equation of motion for  $\phi_2$ . In addition, in an interacting theory, there are terms that are cubic in  $\phi_1$ ,

$$S[\phi_+] - S[\phi_-] = \phi_1 \cdot \frac{\delta S[\phi_2]}{\delta \phi_2} + \text{terms cubic in } \phi_1. \quad (67)$$

We are seeking an approximation that applies in the regime of strong fields, e.g. when the fields are excited by a large external source like in the CGC framework, which implies that  $\phi_2$  is large. Since  $\phi_+$  and  $\phi_-$  are the fields in the amplitude and conjugate amplitude respectively, their difference is a quantum effect whose magnitude is suppressed by  $\hbar$ . Therefore, in such a situation, we have  $\phi_1 \ll \phi_2$ , and it is natural to neglect the cubic term in  $\phi_1$  in the action. After doing this, the field  $\phi_1$  becomes a Lagrange multiplier for the classical equation of motion for  $\phi_2$ . The evolution of  $\phi_2$  is now deterministic, and the only remaining fluctuations are those inherited from the average over the initial density matrix  $\rho_0(\varphi_+^{(i)}, \varphi_-^{(i)})$ . In the Hamiltonian formulation of the classical equation of motion for  $\phi_2$ , the average over  $\varphi_+^{(i)}, \varphi_-^{(i)}$  becomes an average over  $\varphi_2^{(i)}$  and its conjugate momentum  $\Pi_2^{(i)}$ , with a distribution obtained as the Wigner transform of  $\rho_0$ :

$$W_0[\varphi_2^{(i)}, \Pi_2^{(i)}] \equiv \int [D\chi] e^{i \int \chi \cdot \Pi_2} \rho_0(\varphi_2^{(i)} + \frac{\chi}{2}, \varphi_2^{(i)} - \frac{\chi}{2}). \quad (68)$$

### 10.5. CSA in perturbation theory

The path integral derivation of the classical statistical approximation also clarifies what this approximation amounts to in perturbation theory. This knowledge will be useful later when we discuss the non-renormalizability of this approximation. Let us discuss this in the simple framework of a scalar field theory with a  $\phi^4$  interaction term.

The first step is to express the transformation from the  $\phi_{\pm}$  fields to the  $\phi_{1,2}$  fields as a “rotation”, in order to obtain the diagrammatic rules in this new basis.<sup>151–155</sup> From the propagators in the  $\pm$  basis,

$$\begin{aligned} G_{++}^0(p) &= \frac{i}{p^2 - m^2 + i\epsilon}, & G_{--}^0(p) &= \frac{-i}{p^2 - m^2 - i\epsilon} \\ G_{+-}^0(p) &= 2\pi\theta(-p^0)\delta(p^2 - m^2), & G_{-+}^0(p) &= 2\pi\theta(p^0)\delta(p^2 - m^2), \end{aligned} \quad (69)$$

one can define a set of new propagators by a linear transformation on the two indices

$$\mathbb{G}_{\alpha\beta}^0 \equiv \sum_{\epsilon, \epsilon' = \pm} \Omega_{\alpha\epsilon} \Omega_{\beta\epsilon'} G_{\epsilon\epsilon'}^0, \quad (70)$$

with the following transformation matrix

$$\Omega_{\alpha\epsilon} \equiv \begin{pmatrix} 1 & -1 \\ 1/2 & 1/2 \end{pmatrix}. \quad (71)$$

The free rotated propagators are

$$\mathbb{G}_{\alpha\beta}^0 = \begin{pmatrix} 0 & G_A^0 \\ G_R^0 & G_S^0 \end{pmatrix}, \quad (72)$$

where we define

$$G_R^0 = G_{++}^0 - G_{+-}^0, \quad G_A^0 = G_{++}^0 - G_{-+}^0, \quad G_S^0 = \frac{1}{2}(G_{+-}^0 + G_{-+}^0). \quad (73)$$

(The subscripts R, A and S mean respectively for *retarded*, *advanced* and *symmetric*.) Note that the symmetric propagator depends on the initial state of the system, while the retarded and advanced ones are independent of this initial data (they only reflect how modes propagate in the theory under consideration). Under the rotation of eq. (71), the vertices are transformed into

$$\begin{aligned} \Gamma_{1111} &= \Gamma_{1122} = \Gamma_{2222} = 0 \\ \Gamma_{1222} &= -ig^2, \quad \Gamma_{1112} = -ig^2/4. \end{aligned} \quad (74)$$

(The ones not listed explicitly here should be obtained by permutations of the indices.) The CSA simply amounts to setting to zero the vertex  $\Gamma_{1112}$  (and its permutations) wherever it appears in the diagrammatic expansion, while all the other Feynman rules are unmodified.

## 11. Applications of the CSA to heavy ion collisions

The classical statistical approximation has recently been applied to heavy ion collisions in two sets of works, that mostly differ by the nature of the initial conditions that were used.

### 11.1. CGC Initial conditions

In a strict application of the CSA to the description of heavy ion collisions in the Color Glass Condensate framework, the Gaussian ensemble of initial conditions arises from the exponentiation of the 1-loop result. In other words, the CGC description of heavy ion collisions is an initial value problem, and the state of the system at  $\tau = 0^+$  is therefore prescribed uniquely from the fact that the system was in the vacuum state at  $x^0 = -\infty$ . The initial Gaussian ensemble of fields is characterized by the following mean values and variance (written here in a very sketchy way, without color and Lorentz indices):

$$\begin{aligned} \langle \mathcal{A}^\mu \rangle &= \mathcal{A}_{\text{LO}}^\mu \\ \Gamma_2(\mathbf{u}, \mathbf{v}) &= \int \frac{d^2 \mathbf{k}}{(2\pi)^3 2\omega_{\mathbf{k}}} a_{\mathbf{k}}(\tau_0, \mathbf{u}) a_{\mathbf{k}}^*(\tau_0, \mathbf{v}) \\ \left[ \mathcal{D}_\rho \mathcal{D}^\rho \delta_\mu^\nu - \mathcal{D}_\mu \mathcal{D}^\nu + ig \mathcal{F}_\mu{}^\nu \right] a_{\mathbf{k}}^\mu &= 0 \\ \lim_{x^0 \rightarrow -\infty} a_{\mathbf{k}}(x) &= e^{i\mathbf{k} \cdot x}. \end{aligned} \quad (75)$$

The mean value is already known from the LO calculation,<sup>36</sup> given in eqs. (23). From these equations, one sees that the determination of the variance  $\Gamma_2$  amounts to solving the linearized Yang-Mills equations for all the mode functions  $a_{\mathbf{k}}^\mu$  (this formula comes from the derivation of the NLO contribution).<sup>157</sup> As long as we stay in a regime where these perturbations are not yet enhanced by instabilities, the variance is small compared to the mean value squared, and the Gaussian distribution of the initial fields is a narrow distribution centered on the LO color fields (see the right figure 35). The mode functions describe how plane waves with a well defined momentum, color and polarization at  $x^0 = -\infty$  are distorted while they propagate over the LO color background field  $\mathcal{A}_{\text{LO}}^\mu$ . The linearized Yang-Mills equations must be solved for each mode function, up to the time  $\tau_0$  (in the forward light-cone) at which the numerical simulation will start (left figure 35). Explicit formulas for these mode functions were derived in ref.,<sup>157</sup> in the Fock-Schwinger gauge  $A^\tau = 0$  used in these computations. For given quantum numbers :  $\nu$  (the Fourier conjugate of the rapidity  $\eta$ ),  $\mathbf{k}_\perp$ ,  $\lambda$ ,  $c$ , the gauge potential and the associated electrical fields read

$$\begin{aligned} a^i &= \beta^{+i} + \beta^{-i} & a^\eta &= \mathcal{D}^i \left( \frac{\beta^{+i}}{2 + i\nu} - \frac{\beta^{-i}}{2 - i\nu} \right) \\ e^i &= -i\nu (\beta^{+i} - \beta^{-i}) & e^\eta &= -\mathcal{D}^i (\beta^{+i} - \beta^{-i}), \end{aligned} \quad (76)$$

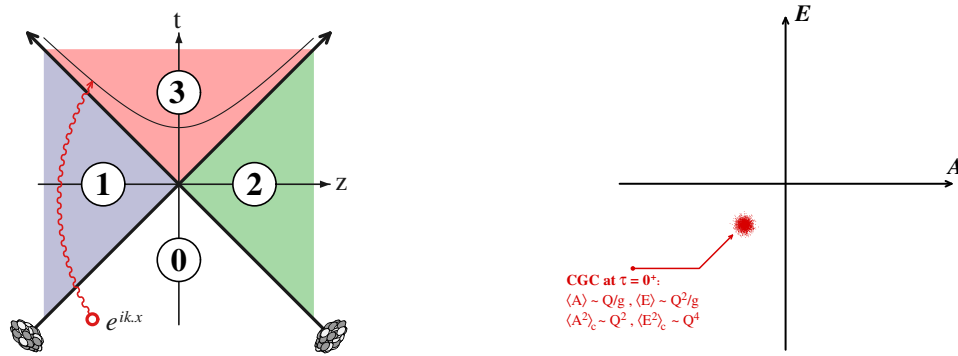


Fig. 35. CGC spectrum of initial fluctuations at  $Q_s \tau_0 \ll 1$ .

where

$$\beta^{+i} \equiv e^{\frac{\pi\nu}{2}} \Gamma(-i\nu) e^{i\nu\eta} U_1^\dagger(\mathbf{x}_\perp) \int_{\mathbf{p}_\perp} e^{i\mathbf{p}_\perp \cdot \mathbf{x}_\perp} \tilde{U}_1(\mathbf{p}_\perp + \mathbf{k}_\perp) \left( \frac{p_\perp^2 \tau}{2k_\perp} \right)^{i\nu} \left( \delta^{ij} - 2 \frac{p_\perp^i p_\perp^j}{p_\perp^2} \right) \epsilon_\lambda^j \tag{77}$$

and

$$\beta^{-i} \equiv e^{-\frac{\pi\nu}{2}} \Gamma(i\nu) e^{i\nu\eta} U_2^\dagger(\mathbf{x}_\perp) \int_{\mathbf{p}_\perp} e^{i\mathbf{p}_\perp \cdot \mathbf{x}_\perp} \tilde{U}_2(\mathbf{p}_\perp + \mathbf{k}_\perp) \left( \frac{p_\perp^2 \tau}{2k_\perp} \right)^{-i\nu} \left( \delta^{ij} - 2 \frac{p_\perp^i p_\perp^j}{p_\perp^2} \right) \epsilon_\lambda^j . \tag{78}$$

$U_{1,2}$  are the Wilson lines that describe the color source content of the two colliding nuclei (they are defined in terms of  $\rho_{1,2}$  in eq. (24)).

These mode functions have been used in ref.<sup>158</sup> in order to compute the time evolution of the components of the energy-momentum tensor from CGC initial conditions. The main difficulty and source of uncertainty in these calculation is the subtraction of the ultraviolet divergences. Firstly, since the energy-momentum tensor is a dimension four operator, it picks up a pure vacuum contribution that behaves as the fourth power of the inverse lattice spacing. This contribution can be removed by subtracting the result of a second computation done with the same lattice parameters, but without the colliding nuclei. A large statistics in the Monte-Carlo evaluation of the average over the initial fields is required for this subtraction. A second kind of ultraviolet contribution, that depends on the background field, was also observed to affect the energy density and the pressure<sup>h</sup>, but not the transverse pressure. Since at this level of approximation, the energy momentum tensor is traceless:

$$\epsilon = P_L + 2P_T , \tag{79}$$

<sup>h</sup>This contribution is possibly due to the non-renormalizability of the CSA – see the subsection 12.1.

and obeys Bjorken's law due to energy-momentum conservation,

$$\partial_\tau(\tau\epsilon) + P_L = 0, \quad (80)$$

the only possible form of an ultraviolet sensitive contribution that does not affect  $P_T$  is a term  $const \times \tau^{-2}$  that affects equally  $\epsilon$  and  $P_L$ . This is indeed what was observed. Lacking a more precise understanding of this term, the constant was fitted in order to subtract this term from  $\epsilon$  and  $P_L$ . After this subtraction, the early time behavior of the ratios  $P_L/\epsilon$  and  $P_T/\epsilon$  closely follows the LO up to  $Q_s\tau \sim 1$ , which is indeed expected since this is before the unstable modes may have affected the time evolution. For a moderately large coupling  $g = 0.5$ , it was found that

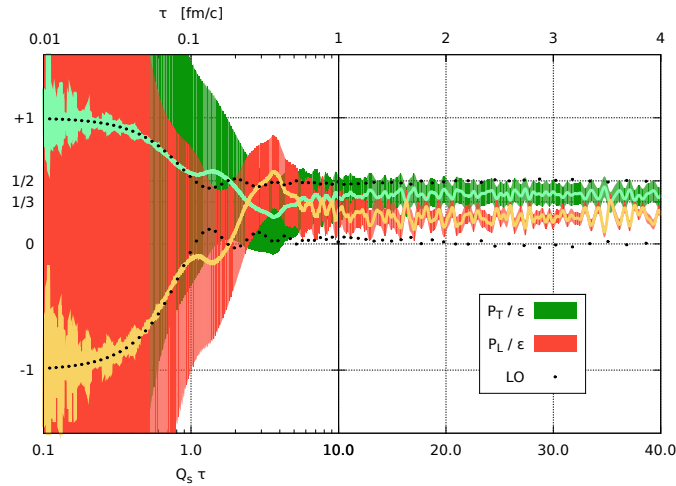


Fig. 36. Behavior of  $P_L/\epsilon$  and  $P_T/\epsilon$  in the CSA with CGC initial conditions. The upper time scale, in  $fm/c$ , is based on a saturation momentum  $Q_s = 2$  GeV.

the longitudinal pressure increases significantly compared to its value in the LO calculation (see the figure 36), and now becomes a sizable fraction of the transverse pressure.

### 11.2. Particle-like initial conditions

Alternatively, one may depart somewhat from the CGC framework and use the same approximation scheme with a different Gaussian ensemble of initial conditions. The simplest model of initial conditions one may consider is an ensemble of fields that describe a distribution of free particles.<sup>159–162</sup> In this case, the center of the Gaussian is  $\mathcal{A}^\mu \equiv 0$ , and the variance is constructed from the in-vacuum mode

functions (derived in<sup>163</sup> for gluons in the Fock-Schwinger gauge) as follows :

$$\langle A^\mu \rangle = 0, \quad \Gamma_2(\mathbf{u}, \mathbf{v}) = \int_{\text{modes } \mathbf{k}} f_0(\mathbf{k}) a_{\mathbf{k}}(\mathbf{u}) a_{\mathbf{k}}^*(\mathbf{v}), \quad a_{\mathbf{k}}(x) \equiv e^{i\mathbf{k}\cdot x}, \quad (81)$$

where  $f_0(\mathbf{k})$  is the initial momentum distribution of these particles. It is plausible that the CGC initial state at  $\tau_0 = 0^+$  may evolve after some time into an incoherent distribution of gluons such as the one described by eqs. (81), but this certainly deserves a thorough study.

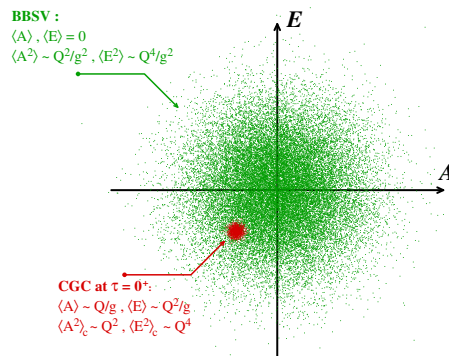


Fig. 37. Illustration of the difference between the initial conditions (75) and (81) for the Wigner distribution of the initial fields.

The difference and complementarity between the initial conditions in eqs. (75) and (81) becomes more transparent if one recalls the symmetric 2-point Green's function in the Schwinger-Keldysh formalism in the presence of a bath of particles,

$$G_s(k) = 2\pi \left( \frac{1}{2} + f_0(\mathbf{k}) \right) \delta(k^2). \quad (82)$$

In this formula, the term in  $f_0(\mathbf{k})$  represents an initial particle distribution, while the term in  $1/2$  corresponds to pure vacuum quantum fluctuations. It thus becomes clear that the CGC initial conditions at  $\tau = 0^+$  can be viewed as vacuum fluctuations that are somewhat altered by the presence of the LO color background field. It is the minimal modification that quantum mechanics can bring to a classical state, promoting it to a (pure) coherent state, while the particle-like initial conditions defined by eqs. (81) are a mixed state from the point of view of quantum mechanics.

This type of particle-like initial condition was used in refs.<sup>159–162</sup> in order to study the evolution of a longitudinally system, in Yang-Mills theory and also in the  $\phi^4$  scalar field theory.<sup>162</sup> Note that, if one chooses an initial distribution proportional to the inverse coupling  $g^{-2}$ , then one can completely scale out the coupling from the calculation by an appropriate rescaling of the fields. In these works, the

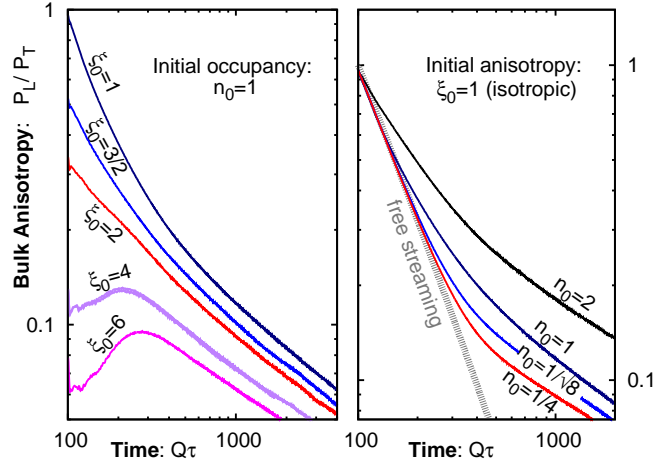


Fig. 38. Behavior of  $P_L/P_T$  in the CSA with particle-like initial conditions in Yang-Mills theory, for various anisotropies ( $\xi_0$ ) and densities ( $n_0$ ) of the initial particle distribution. From Ref.<sup>159</sup>

shape of the initial distribution was controlled by two parameters:  $n_0$  (that controls the overall normalization) and  $\xi_0$  (that controls the anisotropy). Some results regarding the behavior of the ratio  $P_L/P_T$  are shown in the figure 38. Despite substantial variations of these parameters, the system was always observed to reach a scaling regime in which one has the following approximate behaviors,

$$f(\mathbf{p}) \sim \tau^{-2/3} \quad , \quad p_{\perp} \sim \tau^0 \quad , \quad p_z \sim \tau^{-1/3} \quad , \quad \frac{P_L}{P_T} \sim \tau^{-2/3} . \quad (83)$$

Note that these scaling laws are not the free streaming ones (where  $p_z \sim \tau^{-1}$ ,  $f(\mathbf{p}) \sim \tau^0$  and  $P_L/P_T \sim \tau^{-2}$ ) which means that this system interacts significantly but not strongly enough in order to overcome the expansion, at least in the classical approximation. The scaling behavior of the longitudinal momentum  $p_z \sim \tau^{-1/3}$  can be understood semi-analytically<sup>112</sup> if the elastic scattering rate is dominated by small angle scatterings. Quite surprisingly, the same scaling behavior of  $p_z$  was also observed<sup>162</sup> in this approximation in the scalar  $\phi^4$  theory, despite the fact that the leading order scattering cross-section in this theory is dominated by large angle scatterings<sup>1</sup>.

In this approximation, this scaling behavior of eq. (83) will continue forever, and the pressure tensor becomes more and more anisotropic over time. However, since this is a classical approximation, it is known to break at least when the occupation number  $f(\mathbf{p})$  becomes of order one. This is expected to happen when  $Q_s\tau \sim g^{-3}$ , which corresponds to the end of the first stage of the bottom-up scenario of ref.<sup>112</sup> If this scenario –illustrated in the figure 39– is confirmed, the isotropization

<sup>1</sup>See the section 12.3 for a discussion of the possible interplay between the classical approximation and large angle scatterings in anisotropic systems.

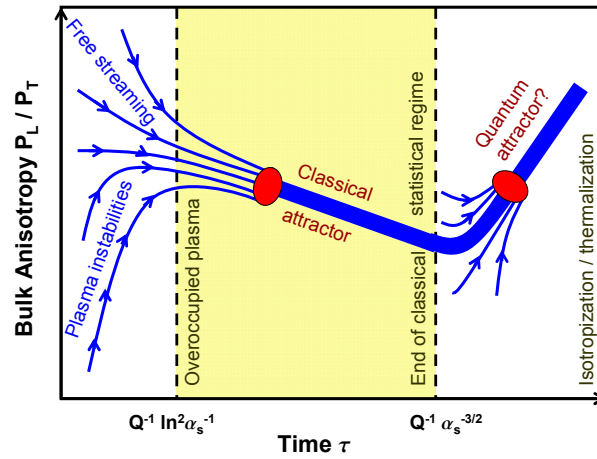


Fig. 39. Thermalization/isotropization scenario that emerges from CSA studies with particle-like initial conditions. From Ref.<sup>159</sup>

of the system would only begin after this time, while the occupation number in the system is no longer large. The quantum corrections would eventually bring the energy-momentum tensor to a quasi-isotropic shape compatible with nearly ideal hydrodynamics. However, what would be more difficult to understand in this scenario is why the shear viscosity to entropy ratio is small. Indeed, in a weak coupling system with occupation numbers of order 1 or below, this ratio is expected to be parametrically large  $\eta/s \sim g^{-4}$ .

## 12. Limitations of the classical statistical approximation

The main appeal of the CSA is the fact that it is quite straightforward to implement, (unlike other schemes like the two-particle irreducible approach, that has never been applied to Yang-Mills theory so far), while at the same time staying very close to the dynamics of the gauge fields so that it is a natural extension of the CGC framework. However, it is not without problems and limitations, that we discuss in this section.

### 12.1. Ultraviolet divergences and non-renormalizability

A very important difference between the initial conditions (75) and (81) is the momentum dependence of the spectrum of field fluctuations. In eqs. (81) the large momentum behavior of the spectrum is controlled by the initial particle distribution  $f_0(\mathbf{k})$ , and therefore it does not extend to infinity if one chooses a  $f_0(\mathbf{k})$  that has a compact support. In contrast, the vacuum fluctuations that are the source of the field fluctuations in the CGC initial conditions have a spectrum which is flat up to  $k = \infty$ .

This difference in the spectra at large momentum leads to very different de-

pendences on the ultraviolet cutoff (i.e. the inverse lattice spacing) in numerical implementations of the CSA using these two types of initial conditions. This issue can be phrased as follows: starting from a renormalizable quantum field theory (e.g. Yang-Mills theory, or a  $\phi^4$  scalar field theory), does the CSA preserve its renormalizability? It turns out that the answer to this question depends on the spectrum of the initial field fluctuations. This can be studied perturbatively<sup>155</sup> by using the retarded-advanced basis, and by using the fact that the CSA amounts to dropping the vertex that has 3 indices of type 1.

From studies performed in the context of quantum field theory at finite temperature,<sup>154,164–167</sup> it has been known for a long time that a particle-like spectrum that falls at least as fast as  $k^{-1}$  leads to a super-renormalizable approximation. In this case, it is sufficient to perform a finite number of subtractions in order to make predictions that do not depend on the ultraviolet cutoff. This applies directly to initial conditions of type (81), provided that the initial distribution  $f_0(\mathbf{k})$  falls quickly enough with momentum.

The situation is quite different with the vacuum-like CGC initial conditions, because they have a flat spectrum of fluctuations. By using the perturbative CSA described in the subsection 10.5, it has been shown in Ref.<sup>155</sup> that the CSA is a non renormalizable approximation of the underlying quantum field theory when this type of initial condition is used. For instance, for the self-energy  $\Sigma_{12}$  at two loops (in a  $\phi^4$  scalar field theory), the CSA gives an ultraviolet divergent result

$$\text{Im} \frac{1}{2} \frac{2}{2} \frac{2}{2} = -\frac{g^4}{1024\pi^3} \left( \Lambda_{\text{UV}}^2 - \frac{2}{3}p^2 \right). \tag{84}$$

Since this divergence occurs in the imaginary part of a correlator, it cannot be removed by a counterterm added to the action (otherwise that would make the action non Hermitian). The consequence of this is that one cannot take the continuum limit in computations based on the CSA with vacuum-like initial conditions. This 2-loop divergence in a self-energy has a counterpart in the classical approximation of the Boltzmann equation, as we shall see in the next subsection.

Non-renormalizable graphs can even be found in some 1-loop 4-point functions,

such as the following  $\Gamma_{1122}$  function :

$$\begin{aligned}
 -i\Gamma_{1122}^{1\text{ loop}} = & \underbrace{\text{S channel}} + \underbrace{\text{T channel}} + \underbrace{\text{U channel}} \quad (85)
 \end{aligned}$$

Here, we have shown all the vertex assignments that would appear in the retarded-advanced basis. Calculating and adding up all these contributions would lead to an ultraviolet finite result, as is expected in a renormalizable theory since the bare Lagrangian has no  $\phi_1^2\phi_2^2$  operator. Note however that some of these graphs contain a 1112 vertex, and would therefore be discarded in the CSA. In this approximation, we only have

$$-i[\Gamma_{1122}]_{\text{CSA}}^{1\text{ loop}} = \text{Diagram 1} + \text{Diagram 2}, \quad (86)$$

the result of which is given by

$$-i[\Gamma_{1122}]_{\text{CSA}}^{1\text{ loop}} = -\frac{g^4}{64\pi} \left[ \text{sign}(t) + \text{sign}(u) + 2\Lambda_{\text{UV}} \left( \frac{\theta(-t)}{|\mathbf{p}_1 + \mathbf{p}_3|} + \frac{\theta(-u)}{|\mathbf{p}_1 + \mathbf{p}_4|} \right) \right], \quad (87)$$

with

$$t \equiv (p_1 + p_3)^2, \quad u \equiv (p_1 + p_4)^2, \quad (88)$$

the standard Mandelstam variables and where  $\Lambda_{\text{UV}}$  is the ultraviolet cutoff on 3-momentum. Despite the zero superficial degree of divergence of these graphs, they contain a linear divergence. Moreover, the coefficient of the divergent terms is non-polynomial in the momenta, implying that it is a non-local ultraviolet divergence. Such non-renormalizable contributions will appear at 2-loops and beyond in the expectation value of inclusive quantities like the energy-momentum tensor. Because of them, CSA calculations performed with initial conditions that contain vacuum

fluctuations should be performed with an ultraviolet cutoff (i.e. the inverse lattice spacing) which is not too large compared to the physical scales.

### 12.2. CSA in kinetic theory

Assessing the cutoff dependence within the CSA itself is very costly, because it requires repeating the same calculation several times with smaller and smaller lattice spacings.<sup>161</sup> A much cheaper way of understanding the interplay between the classical approximation and the dependence on the ultraviolet cutoff is to consider the same approximation at the level of kinetic theory<sup>j</sup>. Let us start with the Boltzmann equation, with the collision term expressed in terms of self-energies in the Schwinger-Keldysh formalism :

$$[\partial_t + \mathbf{v}_p \cdot \nabla] f(p) = \frac{i}{2\omega_p} \underbrace{[f(\mathbf{p})\Sigma_{-+}(P) - (1 + f(\mathbf{p}))\Sigma_{+-}(P)]}_{C_p[f]} . \quad (89)$$

In order to perform in kinetic theory the same approximation as in the CSA, one should first rewrite the collision term in the retarded-advanced basis :

$$C_p[f] = \frac{i}{2\omega_p} \left[ \Sigma_{11}(P) + \left( f(\mathbf{p}) + \frac{1}{2} \right) (\Sigma_{21}(P) - \Sigma_{12}(P)) \right] . \quad (90)$$

( $\Sigma_{11}$  is imaginary, as well as  $\Sigma_{21}(P) - \Sigma_{12}(P)$ ). At this point, we just need to calculate the self-energies that appear in the right hand side (at 2-loops if we want  $2 \rightarrow 2$  collisions) by neglecting the 1112 vertex. The two versions of the CSA, with or without vacuum fluctuations, simply correspond to keeping the  $1/2$  in the factor  $1/2 + f(\mathbf{p})$  that appears in the propagator  $G_{22}$  or not.<sup>174–176</sup> It is easy to check that the classical approximation with no vacuum fluctuations amounts to keeping only the terms that are cubic in the particle distribution, while the classical approximation with vacuum fluctuations leads to the following collision term

$$\begin{aligned} & \frac{g^4}{4\omega_p} \int_{\mathbf{k}} \int_{\mathbf{p}'} \int_{\mathbf{k}'} (2\pi)^4 \delta(P + K - P' - K') \\ & \times \left[ \left( f(\mathbf{p}') + \frac{1}{2} \right) \left( f(\mathbf{k}') + \frac{1}{2} \right) \left( 1 + f(\mathbf{p}) + f(\mathbf{k}) \right) \right. \\ & \left. - \left( f(\mathbf{p}) + \frac{1}{2} \right) \left( f(\mathbf{k}) + \frac{1}{2} \right) \left( 1 + f(\mathbf{p}') + f(\mathbf{k}') \right) \right] , \quad (91) \end{aligned}$$

that has the same cubic and quadratic terms as the exact collision term, but also some spurious terms that are linear in the particle distribution.

<sup>j</sup>Here, we employ kinetic theory as a way to assess some formal aspects of the underlying quantum field theory, like its dependence on the ultraviolet cutoff. A number of works<sup>108–111,168–173</sup> have also used kinetic theory as a tool for studying thermalization in models of heavy ion collisions.

The fixed points of these “classical” Boltzmann equations are

$$\begin{aligned} \text{without vacuum fluctuations :} \quad & f(\mathbf{p}) = \frac{T}{\omega_{\mathbf{p}} - \mu} \\ \text{with vacuum fluctuations :} \quad & f(\mathbf{p}) = \frac{T}{\omega_{\mathbf{p}} - \mu} - \frac{1}{2}, \end{aligned} \quad (92)$$

( $\omega_{\mathbf{p}} \equiv \sqrt{p^2 + m^2}$ ) i.e. respectively the first and the first two terms in the expansion of a Bose-Einstein distribution around low energy.

The parameters  $T$  and  $\mu$  that appear in the asymptotic distributions can be determined from conservation laws. In the Boltzmann equation with only elastic scatterings, both the energy and the particle number are conserved. For the CSA with vacuum fluctuations, these conservation laws lead to

$$\begin{aligned} n &= n_c + \int \frac{d^3\mathbf{p}}{(2\pi)^3} \left( \frac{T}{\omega_{\mathbf{p}} - \mu} - \frac{1}{2} \right) \\ \epsilon &= n_c m + \int \frac{d^3\mathbf{p}}{(2\pi)^3} \omega_{\mathbf{p}} \left( \frac{T}{\omega_{\mathbf{p}} - \mu} - \frac{1}{2} \right). \end{aligned} \quad (93)$$

In this exercise, we allow the formation of a Bose-Einstein condensate with a particle density  $n_c$ , in case one wishes to consider highly populated initial conditions. Note that in any case, there are only two unknowns in these equations:  $T$  and  $\mu$  if there is no condensation, or  $T$  and  $n_c$  if there is condensation (in which case  $\mu = m$ ). From these two equations, we can determine the two unknown parameters. However, since the integrals are ultraviolet divergent, it is necessary to introduce a cutoff  $\Lambda$  on  $|\mathbf{p}|$ , which turns  $T$ ,  $\mu$  and  $n_c$  into  $\Lambda$ -dependent quantities.<sup>156</sup> The

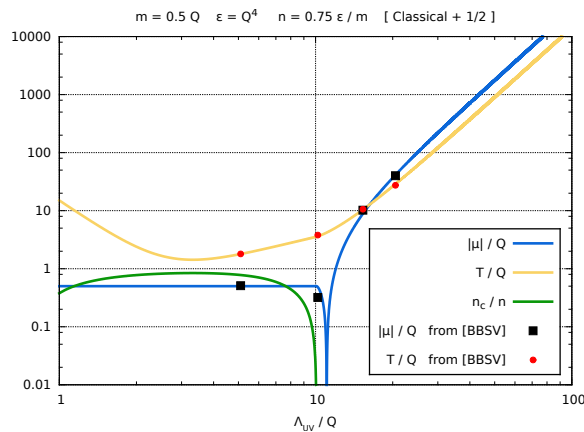


Fig. 40. Evolution of  $T, \mu$  and  $n_c$  as a function of the ultraviolet cutoff. The points reproduce the values listed in the figure 10 of Ref.,<sup>161</sup> obtained with a classical statistical field simulation.

solution of eqs. (93) is shown in the figure 40 ( $Q$  is a physical momentum scale

that characterizes the initial momentum distribution of the particles), where we have also superimposed results from ref.<sup>161</sup> obtained by lattice classical statistical simulations. These curves show a very strong dependence on the ultraviolet cutoff when it becomes much larger than the physical scales, as expected given the fact that the CSA with vacuum fluctuations is not renormalizable. On the other hand, there is a region where the cutoff is a few times the physical scale, and where the parameters that characterize the asymptotic distribution are rather insensitive to the cutoff. Therefore, simulations using the CSA with vacuum fluctuations as initial conditions should preferably be performed with an ultraviolet cutoff chosen in that range, in order to minimize the sensitivity of the results on the cutoff.

### 12.3. Quantum corrections in anisotropic systems

Note that this non-renormalizability problem arises only when one uses the CSA in conjunction with a spectrum of initial conditions that represents vacuum fluctuations, as in eqs. (75). When using particle-like initial conditions, such as those described in eqs. (81), the CSA is ultraviolet finite provided that the initial particle distribution falls faster than  $1/k$ . Because of this, if one forgets that this type of initial condition is not derived directly from the CGC, this implementation of the CSA may seem better since one does not need to worry about the dependence on the ultraviolet cutoff.

However, this choice of initial conditions in the CSA leads to a different kind of problem when used in studies of isotropization in heavy ion collisions, for the following reason. For the purpose of this argument, let us again reason in terms of the Boltzmann equation. For  $2 \rightarrow 2$  collisions, it reads

$$\begin{aligned} \partial_t f_3 \sim g^4 \int_{124} \cdots [f_1 f_2 (f_3 + f_4) - f_3 f_4 (f_1 + f_2)] \\ + g^4 \int_{124} \cdots [f_1 f_2 - f_3 f_4] . \end{aligned} \quad (94)$$

(Here we are tracking the distribution of particles of momentum  $p_3$  – see the figure 41.) In this equation, we have separated the purely classical terms (in  $f^3$ ) from the subleading  $f^2$  terms. When only particle-like fluctuations are included, the CSA applied to the Boltzmann equation keeps only the  $f^3$  terms, and neglects all the other terms. In contrast, the CSA where vacuum fluctuations are included has the  $f^3$  and  $f^2$  terms, and also some unphysical terms that are linear in  $f$  (see Eq. (91)).

Consider now a situation where the particle distribution is strongly anisotropic, with a support in  $p_z$  which is squeezed compared to the support in  $\mathbf{p}_\perp$ . Starting from a generic initial condition of this form, the unapproximated Boltzmann equation will in general lead to isotropization because two purely transverse particles can be scattered outside of the transverse plane<sup>k</sup>. But does this still happen in approximations of the Boltzmann equation? In the figure 41, one has  $p_3^z = -p_4^z \neq 0$ ,

<sup>k</sup>This is obvious in the  $\phi^4$  scalar field theory, where the leading term in the two body cross-section is point-like and where scatterings at large angle are dominant. This is also the case in the CGC,

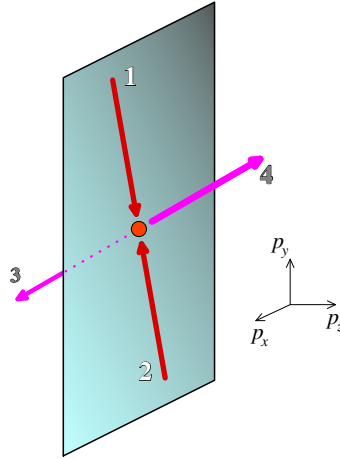


Fig. 41.  $2 \rightarrow 2$  scattering contributing to isotropization.

and given our assumption about the support of the particle distribution, this means that  $f_3 = f_4 \approx 0$ . In the collision term of the Boltzmann equation, a number of terms therefore vanish :

$$\begin{aligned} \partial_t f_3 \sim g^4 \int_{124} \cdots [f_1 f_2 \underbrace{(f_3 + f_4)}_0 - \underbrace{f_3 f_4}_0 (f_1 + f_2)] \\ + g^4 \int_{124} \cdots [f_1 f_2 - \underbrace{f_3 f_4}_0] . \end{aligned} \tag{95}$$

In particular, all the cubic terms are zero. The problem is that these are the only terms that are kept in the CSA with no vacuum fluctuations. The only non-zero term is the term in  $f_1 f_2$ , which would be present in the CSA only if vacuum initial fluctuations are present. From this discussion, the particle-like initial conditions in the CSA, despite their appeal since they lead to UV finite results, may be inappropriate because they lead to missing the most important contribution to isotropization. In other words, in an anisotropic system, the classical approximation could break down long before the occupation number becomes of order 1.

This may also have an incidence on the behavior at intermediate times. With only the  $f^3$  terms, the ratio  $P_L/P_T$  decreases like  $\tau^{-2/3}$  at late times, and therefore the system never isotropizes in this approximation. On the other hand, the system is expected to isotropize eventually with the complete Boltzmann equation ( $f^3$  and  $f^2$  terms), with a ratio  $P_L/P_T \sim \tau^0$  at late times. If the  $f^2$  terms are truly negligible over some extended period of time, then the full Boltzmann equation should lead to the red curve in the figure 42, in which the system spends some time stuck into a thanks to screening. Indeed, since the occupation number is of order  $g^{-2}$ , the Debye mass is of order  $Q_s$ . Since this is comparable to the typical momentum of the gluons, large angle scatterings should be important at early times.

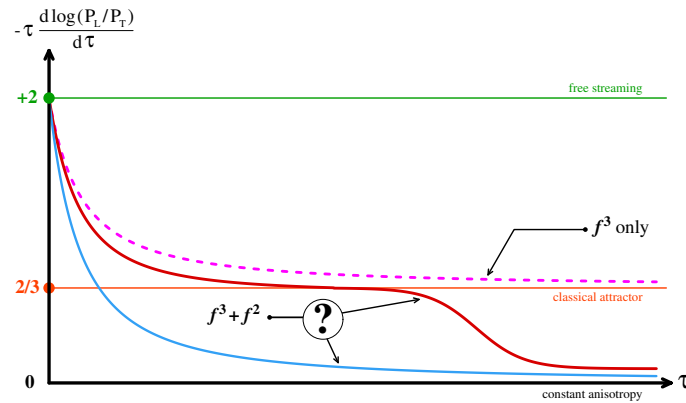


Fig. 42. Behavior of the logarithmic derivative of the ratio  $P_L/P_T$ . Dotted curve: classical approximation where one keeps only the  $f^3$  terms. Red curve: full collision term, if there exists a “classical attractor”. Blue curve: full collision term, if the  $f^2$  terms prevent the classical attractor.

“classical attractor” before eventually leaving it in order to isotropize. In contrast, if the fact that the  $f^2$  terms are always dominant in the tail plays an important role, then one may instead get the blue curve. The Boltzmann equation offers an interesting playground in order to test these possibilities, since it can be solved with and without the  $f^2$  terms at comparable computational costs.

### 13. Summary

A lot of progress has been made in the past 10 years in QCD-based studies of the early stages of heavy ion collisions. The most promising framework for these studies is the Color Glass Condensate, which allows one to systematically include the non-linear effects that prevail when the gluon occupation numbers are large.

The description of the relevant degrees of freedom in the wavefunction of the incoming nuclei and how they evolve as one varies the energy of the collision is entering a very mature stage, since one now knows this evolution at next-to-leading log accuracy. A lot more work will be needed before these NLL evolution equations can be implemented in phenomenological studies of heavy ion collisions, but this is a very important step towards more quantitative results.

Regarding the collision itself, i.e. how two objects described by means of the CGC interact while they collide, one has now a much clearer understanding of how observables can be expressed at leading order in terms of a classical solution of the Yang-Mills equations (and how the inclusive nature of an observable translates into retarded boundary conditions for this classical solution), and how to calculate their next-to-leading order corrections in terms of linearized perturbations around this classical solution.

The recent years have also witnessed a renewed interest in the question of the

isotropization and thermalization of the system produced in heavy ion collisions. This issue has indeed been made more pressing by the many phenomenological successes of hydrodynamical models in describing the expansion of the fireball as a nearly perfect fluid, something which is at odds with the LO CGC results. From recent works, there appears to be two tools of choice for these studies: kinetic theory (in the small scattering angle approximation, or the more sophisticated effective kinetic theory of ref.<sup>105</sup>) and the classical statistical approximation, which is more directly related to the CGC framework. Although this problem seems to have now reached a satisfactory level of understanding—both qualitatively and quantitatively—in the simpler case of a system confined in a fixed volume, the situation is at the moment somewhat unclear in the more realistic situation of a longitudinally expanding system, for which two different results have been obtained in the classical statistical approximation with different initial conditions. These initial conditions mostly differ in whether some vacuum quantum fluctuations are included or not, and a prime question to clarify in the near future will be to understand to what extent quantum fluctuations play a role in isotropization and thermalization.

### Acknowledgements

This work is supported by the Agence Nationale de la Recherche project 11-BS04-015-01.

### References

1. L.V. Gribov, E.M. Levin, M.G. Ryskin, Phys. Rept. **100**, 1 (1983).
2. A.H. Mueller, J-W. Qiu, Nucl. Phys. **B 268**, 427 (1986).
3. J.P. Blaizot, A.H. Mueller, Nucl. Phys. **B 289**, 847 (1987).
4. D.J. Gross, F. Wilczek, Phys. Rev. Lett. **30**, 1343 (1973).
5. D.J. Gross, F. Wilczek, Phys. Rev. **D 8**, 3633 (1973).
6. D.J. Gross, F. Wilczek, Phys. Rev. **D 9**, 980 (1974).
7. H.D. Politzer, Phys. Rev. Lett. **30**, 1346 (1973).
8. H.D. Politzer, Phys. Rept. **14**, 129 (1974).
9. R.P. Feynman, *Photon-Hadron Interactions*, Frontiers in Physics, W.A. Benjamin, (1972).
10. J.C. Collins, D.E. Soper, G. Sterman, Nucl. Phys. **B 250**, 199 (1985).
11. J.C. Collins, D.E. Soper, G. Sterman, Nucl. Phys. **B 261**, 104 (1985).
12. J.C. Collins, D.E. Soper, G. Sterman, Nucl. Phys. **B 263**, 37 (1986).
13. F.D. Aaron, et al, [H1 and ZEUS Collaborations] JHEP **1001**, 109 (2010).
14. G. Altarelli, G. Parisi, Nucl. Phys. **B 126**, 298 (1977).
15. V.N. Gribov, L.N. Lipatov, Sov. J. Nucl. Phys. **15**, 438 (1972).
16. V.N. Gribov, L.N. Lipatov, Sov. J. Nucl. Phys. **15**, 675 (1972).
17. Yu. Dokshitzer, Sov. Phys. JETP **46**, 641 (1977).
18. I. Balitsky, L.N. Lipatov, Sov. J. Nucl. Phys. **28**, 822 (1978).
19. E.A. Kuraev, L.N. Lipatov, V.S. Fadin, Sov. Phys. JETP **45**, 199 (1977).
20. A. Deshpande, R. Ent, R. Milner, CERN Courier, October 2009.

21. E. Iancu, R. Venugopalan, Quark Gluon Plasma 3, Eds. R.C. Hwa and X.N. Wang, World Scientific, hep-ph/0303204.
22. T. Lappi, Int. J. Mod. Phys. **E20**, 1 (2011).
23. H. Weigert, Prog. Part. Nucl. Phys. **55**, 461 (2005).
24. F. Gelis, E. Iancu, J. Jalilian-Marian, R. Venugopalan, Ann. Rev. Part. Nucl. Sci. **60**, 463 (2010).
25. F. Gelis, Int. J. Mod. Phys. **A 28**, 1330001 (2013).
26. L.D. McLerran, R. Venugopalan, Phys. Rev. **D 49**, 2233 (1994).
27. L.D. McLerran, R. Venugopalan, Phys. Rev. **D 49**, 3352 (1994).
28. L.D. McLerran, R. Venugopalan, Phys. Rev. **D 50**, 2225 (1994).
29. F. Gelis, R. Venugopalan, Nucl. Phys. **A 776**, 135 (2006).
30. F. Gelis, R. Venugopalan, Nucl. Phys. **A 779**, 177 (2006).
31. J. Schwinger, J. Math. Phys. **2**, 407 (1961).
32. L.V. Keldysh, Sov. Phys. JETP **20**, 1018 (1964).
33. R.E. Cutkosky, J. Math. Phys. **1**, 429 (1960).
34. G. t'Hooft, M.J.G. Veltman, CERN report 73-9.
35. Yu.V. Kovchegov, Phys. Rev. **D 54**, 5463 (1996).
36. A. Kovner, L.D. McLerran, H. Weigert, Phys. Rev. **D 52**, 6231 (1995).
37. A. Krasnitz, R. Venugopalan, Nucl. Phys. **B 557**, 237 (1999).
38. A. Krasnitz, R. Venugopalan, Phys. Rev. Lett. **84**, 4309 (2000).
39. A. Krasnitz, R. Venugopalan, Phys. Rev. Lett. **86**, 1717 (2001).
40. A. Krasnitz, Y. Nara, R. Venugopalan, Phys. Rev. Lett. **87**, 192302 (2001).
41. A. Krasnitz, Y. Nara, R. Venugopalan, Nucl. Phys. **A 727**, 427 (2003).
42. T. Lappi, Phys. Rev. **C 67**, 054903 (2003).
43. T. Lappi, Phys. Lett. **B 643**, 11 (2006).
44. A. Krasnitz, Y. Nara, R. Venugopalan, Phys. Lett. **B 554**, 21 (2003).
45. A. Krasnitz, Y. Nara, R. Venugopalan, Nucl. Phys. **A 717**, 268 (2003).
46. T. Lappi, R. Venugopalan, Phys. Rev. **C 74**, 054905 (2006).
47. T. Lappi, L.D. McLerran, Nucl. Phys. **A 772**, 200 (2006).
48. A. Dumitru, Y. Nara, E. Petreska, Phys. Rev. **D 88**, 054016 (2013).
49. A. Dumitru, T. Lappi, Y. Nara, Phys. Lett. **B 734**, 7 (2014).
50. A. Ayala, J. Jalilian-Marian, L.D. McLerran, R. Venugopalan, Phys. Rev. **D 53**, 458 (1996).
51. I. Balitsky, Phys. Rev. **D 75**, 014001 (2007).
52. I. Balitsky, G.A. Chirilli, Phys. Rev. **D 77**, 014019 (2008).
53. Yu.V. Kovchegov, H. Weigert, Nucl. Phys. **A 784**, 188 (2007).
54. E. Gardi, J. Kuokkanen, K. Rummukainen, H. Weigert, Nucl. Phys. **A 784**, 282 (2007).
55. A.V. Grabovsky, JHEP **1309**, 141 (2013).
56. I. Balitsky, G.A. Chirilli, Phys. Rev. **D 88**, 111501 (2013).
57. A. Kovner, M. Lublinsky, Y. Mulian, Phys. Rev. **D 89**, 061704 (2014).
58. A. Kovner, M. Lublinsky, Y. Mulian, JHEP **1408**, 114 (2014).
59. J.L. Albacete, N. Armesto, J.G. Milhano, C.A. Salgado, U.A. Wiedemann, Phys. Rev. **D 71**, 014003 (2005).
60. J.L. Albacete, Y. Kovchegov, Phys. Rev. **D 75**, 125021 (2007).
61. J.L. Albacete, N. Armesto, J.G. Milhano, C.A. Salgado, Phys. Rev. **D 80**, 034031 (2009).
62. J.L. Albacete, N. Armesto, J.G. Milhano, C.A. Salgado, arXiv:0906.2721.
63. T. Lappi, H. Mäntysaari, Eur. Phys. J. **C 73**, 2307 (2013).
64. F. Gelis, T. Lappi, R. Venugopalan, Phys. Rev. **D 78**, 054019 (2008).

65. F. Gelis, T. Lappi, R. Venugopalan, Phys. Rev. **D 78**, 054020 (2008).
66. F. Gelis, T. Lappi, R. Venugopalan, Phys. Rev. **D 79**, 094017 (2009).
67. I. Balitsky, Nucl. Phys. **B 463**, 99 (1996).
68. J. Jalilian-Marian, A. Kovner, L.D. McLerran, H. Weigert, Phys. Rev. **D 55**, 5414 (1997).
69. J. Jalilian-Marian, A. Kovner, A. Leonidov, H. Weigert, Nucl. Phys. **B 504**, 415 (1997).
70. J. Jalilian-Marian, A. Kovner, A. Leonidov, H. Weigert, Phys. Rev. **D 59**, 014014 (1998).
71. J. Jalilian-Marian, A. Kovner, A. Leonidov, H. Weigert, Phys. Rev. **D 59**, 034007 (1999).
72. J. Jalilian-Marian, A. Kovner, A. Leonidov, H. Weigert, Phys. Rev. **D 59**, 099903 (1999).
73. E. Iancu, A. Leonidov, L.D. McLerran, Nucl. Phys. **A 692**, 583 (2001).
74. E. Iancu, A. Leonidov, L.D. McLerran, Phys. Lett. **B 510**, 133 (2001).
75. E. Ferreira, E. Iancu, A. Leonidov, L.D. McLerran, Nucl. Phys. **A 703**, 489 (2002).
76. B.I. Abelev, et al., [STAR Collaboration] Phys. Rev. **C 80**, 064912 (2009).
77. A. Dumitru, F. Gelis, L. McLerran, R. Venugopalan, Nucl. Phys. **A 810**, 91 (2008).
78. T. Lappi, S. Srednyak, R. Venugopalan, JHEP **1001**, 066 (2010).
79. S.A. Voloshin, Phys. Lett. **B 632**, 490 (2006).
80. C.A. Pruneau, S. Gavin, S.A. Voloshin, Nucl. Phys. **A 802**, 107 (2008).
81. S. Gavin, L. McLerran, G. Moschelli, Phys. Rev. **C 79**, 051902 (2009).
82. E.V. Shuryak, Phys. Rev. **C 76**, 047901 (2007).
83. J. Adams, et al., [STAR Collaboration] Nucl. Phys. **A 757**, 102 (2005).
84. K. Adcox, et al., [PHENIX Collaboration] Nucl. Phys. **A 757**, 184 (2005).
85. I. Arsene, et al., [BRAHMS collaboration] Nucl. Phys. **A 757**, 1 (2005).
86. B.B. Back, et al., [PHOBOS collaboration] Nucl. Phys. **A 757**, 28 (2005).
87. P. Huovinen, P.V. Ruuskanen, Ann. Rev. Nucl. Part. Sci. **56**, 163 (2006).
88. P. Romatschke, Int. J. Mod. Phys. E **19**, 1 (2010).
89. D. Teaney, Prog. Part. Nucl. Phys. **62**, 451 (2009).
90. P. Romatschke, U. Romatschke, Phys. Rev. Lett. **99**, 172301 (2007).
91. G. Policastro, D.T. Son, A.O. Starinets, Phys. Rev. Lett. **87**, 081601 (2001).
92. G. Policastro, D.T. Son, A.O. Starinets, JHEP **0209**, 043 (2002).
93. M. Martinez, M. Strickland, Nucl. Phys. **A 856**, 68 (2011).
94. M. Martinez, R. Ryblewski, M. Strickland, Phys. Rev. **C 85**, 064913 (2012).
95. W. Florkowski, R. Maj, R. Ryblewski, M. Strickland, Phys. Rev. **C 87**, 034914 (2013).
96. W. Florkowski, R. Ryblewski, M. Strickland, Nucl. Phys. **A 916**, 249 (2013).
97. D. Bazow, U.W. Heinz, M. Strickland, Phys. Rev. **C 90** 5, 054910 (2014).
98. M. Strickland, Nucl. Phys. **A 926**, 92 (2014).
99. M. Nopoush, R. Ryblewski, M. Strickland, Phys. Rev. **C 90**, 014908 (2014).
100. K. Fukushima, F. Gelis, Nucl. Phys. **A 874**, 108 (2012).
101. A. Kurkela, G.D. Moore, JHEP **1112**, 044 (2011).
102. J.P. Blaizot, F. Gelis, J. Liao, L. McLerran, R. Venugopalan, Nucl. Phys. **A 873**, 68 (2012).
103. M.C. Abraao York, A. Kurkela, E. Lu, G.D. Moore, Phys. Rev. **D 89**, 074036 (2014).
104. A. Kurkela, E. Lu, Phys. Rev. Lett. **113**, 182301 (2014).
105. P. Arnold, G.D. Moore, L.G. Yaffe, JHEP **0301**, 030 (2003).
106. T. Epelbaum, F. Gelis, Nucl. Phys. **A 872**, 210 (2011).
107. J. Berges, D. Sexty, Phys. Rev. Lett. **108**, 161601 (2012).

108. J.P. Blaizot, J. Liao, L.D. McLerran, Nucl. Phys. **A 920**, 58 (2013).
109. F. Scardina, D. Perricone, S. Plumari, M. Ruggieri, V. Greco, Phys. Rev. **C 90** 5, 054904.
110. Z. Xu, K. Zhou, P. Zhuang, C. Greiner, Phys. Rev. Lett. **114** 18, 182301 (2015).
111. X.G. Huang, J. Liao, Int. J. Mod. Phys. **E23**, 1430003 (2014).
112. R. Baier, A.H. Mueller, D. Schiff, D. Son, Phys. Lett. **B 502**, 51 (2001).
113. A. Kurkela, G.D. Moore, JHEP **1111**, 120 (2011).
114. P. Romatschke, R. Venugopalan, Phys. Rev. Lett. **96**, 062302 (2006).
115. P. Romatschke, R. Venugopalan, Eur. Phys. J. **A 29**, 71 (2006).
116. P. Romatschke, R. Venugopalan, Phys. Rev. **D 74**, 045011 (2006).
117. T.S. Biro, C. Gong, B. Muller, A. Trayanov, Int. J. Mod. Phys. **C 5**, 113 (1994).
118. U.W. Heinz, C.R. Hu, S. Leupold, S.G. Matinyan, B. Muller, Phys. Rev. **D 55**, 2464 (1997).
119. J. Bolte, B. Müller, A. Schäfer, Phys. Rev. **D 61**, 054506 (2000).
120. H. Fujii, K. Itakura, Nucl. Phys. **A 809**, 88 (2008).
121. H. Fujii, K. Itakura, A. Iwazaki, Nucl. Phys. **A 828**, 178 (2009).
122. T. Kunihiro, B. Muller, A. Ohnishi, A. Schafer, T.T. Takahashi, A Yamamoto, Phys. Rev. **D 82**, 114015 (2010).
123. S. Mrowczynski, Phys. Lett. **B 314**, 118 (1993).
124. S. Mrowczynski, Phys. Lett. **B 393**, 26 (1997).
125. A.K. Rebhan, P. Romatschke, M. Strickland, Phys. Rev. Lett. **94**, 102303 (2005).
126. A.K. Rebhan, P. Romatschke, M. Strickland, JHEP **0509**, 041 (2005).
127. S. Mrowczynski, A. Rebhan, M. Strickland, Phys. Rev. **D 70**, 025004 (2004).
128. P. Romatschke, M. Strickland, Phys. Rev. **D 68**, 036004 (2003).
129. P. Romatschke, M. Strickland, Phys. Rev. **D 70**, 116006 (2004).
130. A.K. Rebhan, D. Steineder, Phys. Rev. **D 81**, 085044 (2010).
131. A.K. Rebhan, M. Strickland, M. Attems, Phys. Rev. **D 78**, 045023 (2008).
132. P. Arnold, J. Lenaghan, G.D. Moore, JHEP **0308**, 002 (2003).
133. P. Arnold, J. Lenaghan, G.D. Moore, L.G. Yaffe, Phys. Rev. Lett. **94**, 072302 (2005).
134. P. Arnold, G.D. Moore, Phys. Rev. **D 73**, 025013 (2006).
135. P. Arnold, G.D. Moore, Phys. Rev. **D 73**, 025006 (2006).
136. P. Arnold, G.D. Moore, Phys. Rev. **D 76**, 045009 (2007).
137. P. Arnold, G.D. Moore, L.G. Yaffe, Phys. Rev. **D 72**, 054003 (2005).
138. A. Dumitru, Y. Nara, M. Strickland, Phys. Rev. **D 75**, 025016, (2007).
139. D. Bodeker, K. Rummukainen, JHEP **0707**, 022 (2007).
140. J. Berges, D. Gelfand, S. Scheffler, D. Sexty, Phys. Lett. **B 677**, 210 (2009).
141. J. Berges, S. Scheffler, D. Sexty, Phys. Rev. **D 77**, 034504 (2008).
142. M. Attems, A. Rebhan, M. Strickland, Phys. Rev. **D 87**, 025010 (2013).
143. K. Fukushima, Phys. Rev. **C 75**, 021902 (2007); Erratum: arXiv:0711.2634.
144. K. Dusling, T. Epelbaum, F. Gelis, R. Venugopalan, Nucl. Phys. **A 850**, 69 (2011).
145. P.B. Greene, L. Kofman, A.D. Linde, A.A. Starobinsky, Phys. Rev. **D 56**, 6175 (1997).
146. D. Polarski, A.A. Starobinsky, Class. Quant. Grav. **13**, 377 (1996).
147. D.T. Son, hep-ph/9601377.
148. S.Yu. Khlebnikov, I.I. Tkachev, Phys. Rev. Lett. **77**, 219 (1996).
149. R. Micha, I.I. Tkachev, Phys. Rev. **D 70**, 043538 (2004).
150. K. Fukushima, F. Gelis, L. McLerran, Nucl. Phys. **A 786**, 107 (2007).
151. P. Aurenche, T. Becherrawy, Nucl. Phys. **B 379**, 259 (1992).
152. M.A. van Eijck, R. Kobes, Ch.G. van Weert, Phys. Rev. **D 50**, 4097 (1994).
153. F. Gelis, Nucl. Phys. **B 508**, 483 (1997).

154. G. Aarts, J. Smit, Nucl. Phys. **B 511**, 451 (1998).
155. T. Epelbaum, F. Gelis, B. Wu, Phys. Rev. **D 90** 6, 065029 (2014).
156. T. Epelbaum, F. Gelis, N. Tanji, B. Wu, Phys. Rev. **D 90** 12, 125032 (2014).
157. T. Epelbaum, F. Gelis, Phys. Rev. **D 88**, 085015 (2013).
158. T. Epelbaum, F. Gelis, Phys. Rev. Lett. **111**, 232301 (2013).
159. J. Berges, K. Boguslavski, S. Schlichting, R. Venugopalan, Phys. Rev. **D 89**, 074011 (2014).
160. J. Berges, K. Boguslavski, S. Schlichting, R. Venugopalan, Phys. Rev. **D 89**, 114007 (2014).
161. J. Berges, K. Boguslavski, S. Schlichting, R. Venugopalan, JHEP **1405**, 054 (2014).
162. J. Berges, K. Boguslavski, S. Schlichting, R. Venugopalan, Phys. Rev. Lett. **114** 6, 061601 (2015).
163. K. Dusling, F. Gelis, R. Venugopalan, Nucl. Phys. **A 872**, 161 (2011).
164. D. Bodeker, L.D. McLerran, A. Smilga, Phys. Rev. **D 52**, 4675 (1995).
165. P. Arnold, D.T. Son, L.G. Yaffe, Phys. Rev. **D 55**, 6264 (1997).
166. G. Aarts, J. Smit, Phys. Lett. **B 393**, 395 (1997).
167. G. Aarts, B.J. Nauta, C.G. van Weert, Phys. Rev. **D 61**, 105002 (2000).
168. M. Ruggieri, F. Scardina, S. Plumari, V. Greco, Phys. Rev. **C 89**, 054914 (2014).
169. A. Puglisi, S. Plumari, V. Greco, arXiv:1407.2559.
170. A. Puglisi, S. Plumari, V. Greco, Phys. Rev. **D 90** 11, 114009 (2014).
171. J. Uphoff, O. Fochler, F. Senzel, C. Wesp, Z. Xu, C. Greiner, Phys. Rev. Lett. **114** 11, 112301 (2015).
172. O. Fochler, J. Uphoff, Z. Xu, C. Greiner, Phys. Rev. **D 88**, 014018 (2013).
173. M. Greif, I. Bouras, Z. Xu, C. Greiner, Phys. Rev. **D 90**, 094014 (2014).
174. A.H. Mueller, D.T. Son, Phys. Lett. **B 582**, 279 (2004).
175. S. Jeon, Phys. Rev. **C 72**, 014907 (2005).
176. V. Mathieu, A.H. Mueller, D.N. Triantafyllopoulos, Eur. Phys. J. **C 74**, 2873 (2014).